Self-organized dendritic sidebranching in directional solidification: Sidebranch coherence within uncorrelated bursts

Alain Pocheau, Simona Bodea, and Marc Georgelin
IRPHE, Aix-Marseille Université and CNRS, 49 rue Joliot-Curie, BP 146, Technopôle de Château-Gombert, F-13384 Marseille, France
(Received 18 June 2009; published 3 September 2009)

We experimentally study the level of organization of dendritic sidebranching in directional solidification. For this, we extract successive interface positions at a fixed distance from the dendrite tips and we perform various correlation analyses. The sidebranching signals appear composed of randomly distributed bursts in which sidebranching coherence is surprisingly large and robust. This is attested by the large autocorrelation found in single bursts and the large cross-correlation found in any couple of bursts, even belonging to different sides of a dendrite or to different dendrites. However, the phase coherence of sidebranching breaks down at the transition between bursts. This restricts the coherence of extended sidebranching signals to a mean burst length and prevents the occurrence of large scale cross-correlation between them. This balanced view on sidebranching coherence stresses the capability of self-organization of dendrites in material science and sheds light on the nature of sidebranching on curved growing forms.

DOI: 10.1103/PhysRevE.80.031601 PACS number(s): 68.70.+w, 82.40.Ck, 47.20.Hw

I. INTRODUCTION

The growth forms displayed in nature or in industry usually depart from flatness due to instabilities, large amplitude disturbances, or external forcing. They thus involve curvature as displayed for instance by meristems [1], icicles [2], viscous digits [3], solidification dendrites [4], or flame fronts [5]. Interestingly, whatever its magnitude, curvature proves to be essential in making small scale distortions glide and stretch along the growing form. This kinematic effect then largely modifies the development of instabilities, the elementary distortions being no longer amplified at a fixed place as on a planar form but instead drifted and stretched along the curved interface at the course of their amplification. The resulting dynamics may then display different kinds of organizations depending on the system. In particular, its outcomes range from the well-ordered phylotactic organizations displayed by growing protrusions on plant meristems [6] to the irregular distributions of sidebranches reported in free solidification [7–9] with, in between, the regular cellular tip splittings displayed on radial growth of bacterial colonies [10] or on directional solidification of curved interfaces [11].

This large variety of ordering shows that curvature may help—or may fail—in making some self-organization spontaneously emerge from instabilities. To improve the analysis of the important issues attached to this alternative and the identification of the possible relevant scenarios, it is useful to draw attention on well-known physical systems involving a firm and cross-checked modeling. One of them is the directional solidification of a material from its melt for which the physical foundations of interface dynamics is actually deeply rooted [12,13]. We thus propose here to experimentally address the level of organization of dendritic sidebranching in this directional growth system. A second motivation comes from the fact that beyond the above general issue, sidebranching also provides important implications in material sciences where dendrites stand as a canonical microstructure of metallurgy [14] which may even be used as a tool for building ceramics with enhanced physical properties [15]. Interestingly, studying it here will provide a balanced view on the self-organization of dendritic sidebranching including both uncorrelated sidebranch bursts and an impressively large sidebranch correlation within each [16].

Coming from the Greek "dendron" for "tree," the term dendrite refers to a growing needle form on which lateral protrusions are successively emitted. This results in a treelike shape on which sidebranches emerge from a main trunk (Fig. 1). This kind of forms may be encountered in issues as different as neuron morphology [17], electrodeposition [18], or solidification [19] and will be considered here in the context of solidification [20]. Here, the needle forms which provide dendrites result from the primary instability of a planar front [12]. They first appear as smooth, unbranched, digit cells but, following a secondary instability, further develop sidebranches above a size-dependent velocity threshold [21]. This results in the formation of the paramount microstructure of dilute alloys: the dendrite. As for other kinds of dendrites, the level of organization of their sidebranch trains stands as an outstanding question. It is all the more relevant that the form of the directional solidification interfaces monitors the modulations of solute concentration in the solidified materials and, thus, their resulting physical properties. However,

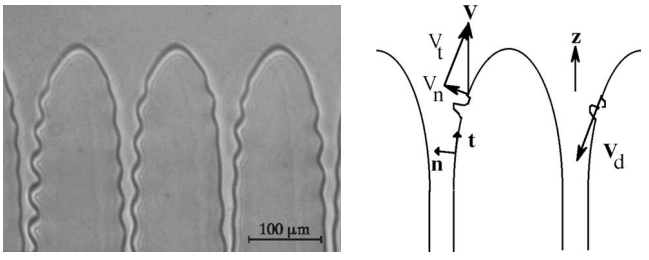

FIG. 1. Image of a directional dendrite (a) and sketch of the kinematic drift undergone in the dendrite frame by modulations growing normally to the interface (b). Here $\mathbf{V}=V_n\mathbf{n}+V_t\mathbf{t}$ is the solidification velocity of the steadily growing needle form, $V_n\mathbf{n}$ the solidification velocity of the normally growing modulations, and $\mathbf{V}_d=V_n\mathbf{n}-\mathbf{V}=-V_t\mathbf{t}$ their resulting drift velocity in the dendrite frame.

the actual nature of the self-organization of sidebranches still remains controversial, since both regular or noisy organizations are predicted by theories [22–32] and observed in experiments [7–9,33–42].

In this paper, we aim at clarifying the level of organization of dendritic sidebranching in directional solidification. For this, we perform a directional solidification experiment of a transparent material in a thin sample and we record the sidebranching signals over long times. This enables us to perform accurate correlation studies in various ways so as to identify those parts of the signals that display some organization. It then appears that dendritic sidebranches are coherently emitted inside uncorrelated and randomly distributed sidebranch bursts. This ambivalence provides a new picture of sidebranch emission which stresses the actual, albeit limited, capability of spontaneous self-organization of dendrites in material science.

The paper is organized as follows. In Sec. II, we recall the different mechanisms proposed so far for sidebranching and the different features reported on it experimentally. We then draw on the corresponding alternatives regarding the nature of sidebranching. In Sec. III, we describe the experimental setup and the techniques used for analyzing the sidebranching signals. Section IV is then devoted to a global analysis of the dendritic signals from which two characteristic time scales emerge: that of the sidebranch emissions and that of the burst emissions. Correlation analyses of sidebranch emissions within single bursts and over a range of bursts are performed in Sec. V and Sec. VI, respectively. They are completed in Sec. VII by a study of the phase coherence between neighbor bursts and in Sec. VIII by a study of sidebranching coherence in the strong sidebranching regime and on asymmetric dendrites. This is followed by a discussion and a conclusion on these sidebranching features.

II. NATURE OF SIDEBRANCHING DYNAMICS: AN ALTERNATIVE

The main differences regarding the development of a perturbation on a needle form as compared to that on a planar interface stem from an additional drift away from the needle tip. This drift appears as a direct kinematic consequence of the variation in normal directions on the curved needle form, following which a protrusion growing normally to the interface regularly increases its distance to the tip [Fig. 1(b)]. In particular, for a needle form growing steadily at velocity $\mathbf{V}$ on a direction $\mathbf{z}$, the normal velocity V_n of its points satisfies $\mathbf{V}=V_n\mathbf{n}+V_t\mathbf{t}$, the vectors $\mathbf{n}$ and $\mathbf{t}$ denoting the interface normal and the interface tangent and V_t the tangential velocity of the moving points. This implies that protrusions growing normally to the interface also glide at a velocity $\mathbf{V}_d=V_n\mathbf{n}-\mathbf{V}=-V_t\mathbf{t}$ along the needle form, as soon as $\mathbf{z}\cdot\mathbf{t}\neq 0$, i.e., as soon as the interface is curved.

This kinematic drift of growing disturbances brings about two main implications regarding their development. At first, their amplification time until disappearing in the dendrite groove gets finite. This raises the difficulty of handling a long-time prediction for a phenomenon made of individually finite repetitive events. The second implication is that a growing disturbance visits different environments at the course of its development, e.g., different temperatures, solute concentrations, and normal growth directions. This makes its growth a heterogeneous issue which requires a knowledge of the whole needle form to be addressed. The differences between the theoretical scenarios proposed for sidebranching refer to a different handling of these issues. Although they have mainly been considered in free growth, they provide relevant frameworks for application to directional growth.

The first theoretical scheme for sidebranch development has been proposed in premixed combustion [22]. The goal was to understand why sufficiently curved flames are stable whereas more flat ones are destroyed by a too large flattering of their sides. It has then been transposed to solidification in a slightly different perspective consisting in addressing the long-time behavior of needle forms that actually survive to sidebranch development [23]. The underlying vision of sidebranching which supports this scenario is that the successive sidebranch emissions correspond to successive resets of the sidebranch dynamics. In particular, any new sidebranch is considered as being independent of the surrounding ones so that its development may be determined by following its drift toward the dendrite grooves while ignoring the other branches. This turns out treating sidebranching as a convective instability in which the amplification of perturbations is addressed in the frame comoving with a disturbance. Within a WKB approximation and a linearized dynamics, the net growth factor of disturbances can then be evaluated as an integral contribution of their linear growth rates over their development stage [22,23]. The inhomogeneity of solidification fields calls for parametrizing the local conditions encountered by growing disturbances and for taking into account the wavelength stretch induced by the tangential velocity gradient. This convective approach of sidebranching has finally been transposed to directional solidification with essentially similar kinds of conclusions [28].

Another kind of convective theory has been simultaneously developed by considering the normal modes of propagation of disturbances on the solidification interface [24–27,32]. Here the interface is considered as a whole but still in a linearized approach of perturbation dynamics in which the trains of disturbances are treated as wave packets of disturbances [24–27]. It is then found that, following the spatial inhomogeneity of interface dynamics, the most amplified wave changes wave number as it drifts to the grooves, thus resulting in a selective amplification of perturbations.

As these convective scenarios deny long-time coupling in favor of repetitive resets of linear amplication, as seen from a fixed location, they yield a phase uncorrelation between branches which simply reflects that of the noisy perturbations from which they grew. They thus provide a mechanism by which sidebranching behaves as a noise amplifier of disturbances yielding uncorrelated sidebranches.

A second kind of scenario emphasizes that, for some reasons, noticeable couplings may occur between successive sidebranches, either directly or by means of their common environment [29–31]. The finite time of amplication of a disturbance may then be overlooked since some information can pass from one disturbance to the next eventually ending to a sustained permanent dynamical state. The duration of

this global state being infinite, it necessarily involves nonlinear features which are expected to yield a limit cycle. Then dendrite behaves as a nonlinear oscillator. This results in a largely modified picture of sidebranching involving a nonlinear oscillating state anchored to the needle form within which disturbances drift and grow. In particular, the overall coherence of the nonlinear oscillator goes together with a large correlation of sidebranches.

In between the noise-amplifier scenario and the nonlinear oscillator scenario stands the interfacial wave theory [32]. Here, a permanent oscillating state of the solidification interface is sought in the linear regime of amplification. An imaginary part of the growth rates of eigenmodes combined with a positive real part is then sought through a Hopf bifurcation. The existence of turning points in the dispersion relation, however, gives rise to a trapping of disturbance waves in the tip region and thus to a possible feedback loop between the dendritic interface and the dendrite tip. As a result, a permanent dynamical state may emerge from noise with possible phase correlation between sidebranches. However, as the nonlinear development of the Hopf instability stands beyond the scope of the analysis, the ultimate fate of the system remains undetermined.

The following alternative, therefore, emerges regarding sidebranching: noise amplifier or nonlinear oscillator. It actually relies on whether the coherence time of the dynamics is restricted to a sidebranch development or to a series of sidebranch development. This is reminiscent of the situation encountered in fluid mechanics where the nature of the dynamics of bluff-body wakes follows from either a convective or an absolute instability [43]. In the former case, analysis is laid on the growth of a disturbance in its comoving frame with no relevant coupling with the surrounding medium: this provides a noise amplifier. In the latter case, analysis is made in the wake frame with disturbances passing through: this provides organized states as the Bénard–von Kármán vortex wakes. The conditions enabling to go from one to the other outcome may be identified provided the underlying system involves a sufficiently accurate modeling [44].

Most experiments on sidebranching have been performed on free growth in pure materials [9,33,34] and alloys [8,35–41] or on viscous digitation [42]. Unfortunately, they provide a controversial view which does not allow the selection of a definitive outcome for the above alternative. Depending on the study, sidebranching is reported to be uncorrelated [9], partly correlated [8], or largely correlated [36]. The material was pure in the former case and a melt in the two latter cases. Interestingly, the observed correlations were found not only on each side of dendrites but also between both their sides [8,36]. In particular, in the partly correlated case [8], a normalized cross-correlation function $C(\tau)$, $0 \leq |C(\tau)| \leq 1$, between the right and left sides of a dendrite decreased from $C(0)=0.4$ at zero delay τ to $C(\tau)=0$ over a correlation time of six sidebranching periods. There, a large value of $C(0)$ noticeably different from zero denotes a definite cross-correlation between both sides of the dendrite. Also, in the largely correlated case [36], the long-time correlation of sidebranching on a dendrite side goes together with a nearly mirror symmetry between both sides of dendrites.

Other relevant differences between the conclusions of free growth experiments refer to an essential dynamical feature: the dendrite tip dynamics. Tip velocities are thus reported to be steady [8,9,36–38] or oscillating [33–37,39–41] and tip curvature radii are found to be constant [8,9] or time periodic [36,37,39]. Some of these differences may refer to the conditions of observation, e.g., to the accuracy of tip velocity measurements or to the extension of the domain in which curvature radii are determined.

Experiments in forced environments have been conducted in both free [45–47] and directional [48] growth with periodic thermal [47,48], hydrodynamic [45,46] or mechanical [47] perturbations. In line with Floquet's theory, dendrites then adopted a time-periodic dynamics at the modulation frequency. The study of the development of sidebranch amplitude along the needle form then provided a wave number dependence of the growth factor which agreed with that expected from the planar instability in a WKB approximation [45,46,48]. Similar findings have finally been derived on viscous digits periodically excited at their tip by a tiny bubble [42].

As compared to free growth, the nature of sidebranching in directional solidification gave rise to less investigations. However, on the theoretical side, the appearance of sidebranches on cells for increasing velocity has been linked to a transition between two distinct branches of solutions for directional solidification: a cell branch and a dendrite branch involving different mean geometrical features [49]. This would be accompanied by a finite change in geometrical properties (e.g., curvature radius or spacing) and would thus correspond to a first-order transition. This scenario was in line with a sudden increase in spacing reported by metallurgists at the cell to dendrite transition [50]. However, this increase refers to the mean spacing of microstructures on the solidification interface instead of the actual spacing of those cells that undergo the transition. Further observations of cell dynamics then showed that it actually referred not to the cell to dendrite transition but to another phenomenon, a cell elimination instability, that reduces the cell spacings in the same velocity range [51,52].

On the other hand, in the same experimental setup as that used here and in the same material, we previously noticed that the geometry of microstructures suffers no abrupt change at the sidebranching transition [21,53]. In particular, it showed a continuous variation in the curvature radius [54] and a constant spacing. This points to a second-order transition related to a supercritical instability. We then identified the related critical surface which delimits in the parameter space the unstable domain where sidebranches are noticeable from the stable domain where they are not [21]. As the noise level is presumed to be the same on all microstructures and the resolution of observation was kept constant on the whole study, the transition between both domains should refer to the same value of the net growth factor induced by a convective instability. The expression of this growth factor has been determined in the context of directional solidification [28], thus allowing comparison between theory and experiment. However, quantitative comparison between experimental data and noise-amplification predictions revealed discrepancies far beyond experimental accuracy [52,55].

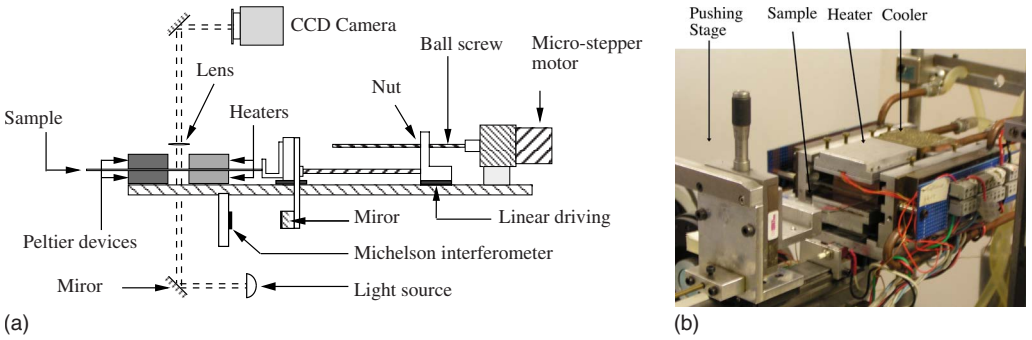

FIG. 2. (Color online) Experimental setup. (a) Sketch showing the thermal, mechanical, and optical parts. (b) Snapshot of the main stages.

This disagreement regarding the localization of the sidebranching transition in the parameter space is all the more surprising that the vanishingly small sidebranch amplitude at this transition corresponds to the best condition for the relevance of the growth factor derivation. It thus sheds doubt on the relevance of a convective instability to explain sidebranching. As a support, the observed dendrites qualitatively seemed to be more ordered than expected from a noise amplification mechanism [21]. These statements then call for directly investigating the nature of the correlation between the sidebranches of actual dendrites to help clarifying the relevance of noise-amplification as opposed to nonlinear oscillation.

III. EXPERIMENTAL SETUP AND METHODS

The experimental setup aims at providing the directional solidification of a transparent material together with the direct nonintrusive observation of the solidification interface. It has been designed so as to ensure a fine control of the solidification conditions. The data provided by the sidebranching images have then been analyzed so as to determine the level of correlations between branches.

A. Experimental setup

The setup is made of a mechanical stage which pushes a thin sample of alloy into a thermal stage where solidification takes place (Fig. 2). Samples are made of two glass plates, 150 mm long, 45 mm wide, and spaced by 50 μm thick mylar bands. They are filled with a transparent dilute alloy of succinonitrile with an ethylenic solute. As this plastic material provides rough interfaces, it may be used to mimic the solidification of metals with a lower melting point: $T_M = 58.08$ K for pure succinonitrile [4]. Infrared and nuclear magnetic resonance analyses reveal that impurities involve an ethylenic chemical bond and no hydroxyl bond. This points to ethylen (or its cyano monosubstituted derivative acrylonitrile) as solute and excludes contamination by water. Measurements of the physical features of the melt give solutal diffusion coefficient $D = 1350 \pm 50$ μm^2 s^{-1}, partition coefficient $k = 0.29 \pm 0.05$, impurity concentration $c_\infty = 1.5$ mol %, and critical velocity $V_c = 1.7$ μm s^{-1} at the thermal gradient $G = 78$ K cm^{-1} mainly used in this study. Succinonitrile solidifies as a body-centered-cubic crystal. Prior to solidification, a definite crystalline orientation is carefully selected by making an appropriate grain invade the whole sample. It was chosen so as to fit the main experiment axes, the principal $\langle 100 \rangle$ axes being aligned with the sample depth, the thermal gradient, and the isothermal lines. This way, symmetrical dendrites growing along the thermal gradient direction are expected [56].

The thermal stage is made of a pair of heaters and coolers sandwiching the sample. Heaters are made of copper blocks heated by a resistive sheet and coolers are made of stainless blocks including a Peltier device to transport heat to a water circulation. All devices include thermal probes and are electronically regulated to better than 0.1 K. Heaters and coolers temperatures are fixed at 100 °C and 10 °C, respectively. They are separated by a gap g in between 5–15 mm yielding an effective thermal gradient of 50–140 K cm^{-1} at the solidification interface. The thermal diffusivity of the sample glass plates is $\kappa = 5 \times 10^5$ μm^2 s^{-1}. This provides a thermal diffusion time $\tau_d = g^2/\kappa$ of about $\tau_d = 200$ s in the sample which acts as a low-pass filter for perturbations (Appendix).

The mechanical stage is composed of a microstepper motor which induces the rotation of a 5 mm pitch ball screw and the resulting translation of a nut on a linear track. The nut then transfers its motion to the sample through a pushing stage. A special attention has been provided to the regularity of the sample velocity. For this, the motor is fixed on micropositionners that allow an accurate alignment of its axis on the track. It involves 200 steps per turn and 32 microsteps per step, at the end of which Foucault currents slow rotation to prevent vibration. The regularity of the sample translation is controlled by Michelson interferometry to an accuracy of 0.2 micron. This corresponds to an accuracy on sample velocity of 5×10^{-2} μm s^{-1} on a sidebranching period of 4 s and of 6×10^{-3} μm s^{-1} on a burst period of about 35 s.

Such a large accuracy enabled us to control the linearity of the sample translation all over the experiment. High frequency vibrations at about 100 Hz were detected around the resonance frequency of the Michelson mirror arm. They thus presumably refer more to the measurement device than to the solidification setup. Anyway, compared to the sidebranch frequency which is smaller than a hertz, this vibration frequency appears too large to induce noticeable effects on solidification dynamics. On the other hand, small modulations were found at the period of a screw turn, i.e., about every 330 s at a translation velocity of 15 μm s^{-1}. They were

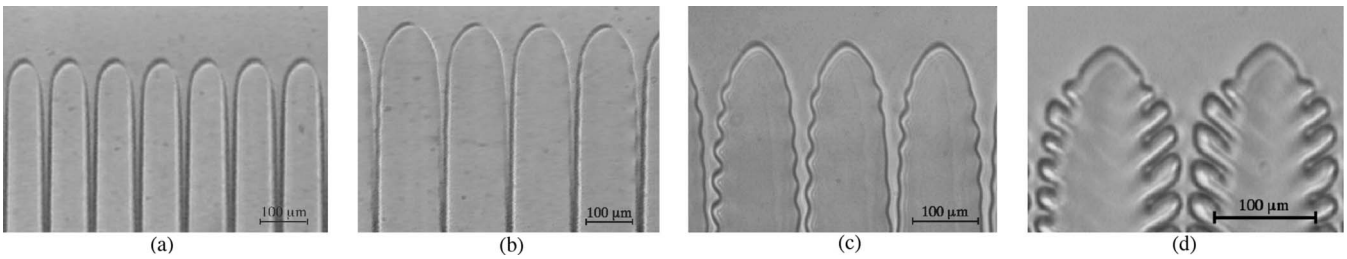

FIG. 3. Successive microstructures displayed when increasing the velocity: (a) Cells. (b) Dendrites at the onset of sidebranching. (c) Dendrites in the moderate sidebranching regime. (d) Dendrites in the strong sidebranching regime.

minimized by a fine alignment of the different parts of the device and reduced to quasisinusoidal modulations of relative amplitude $\delta V/V$ smaller than $\pm 3\%$ at most.

Observation of the solidification interface is made by ombroscopy. A parallel light beam undergoes optical aberrations when crossing the interface. It then enables the interface to be visualized as a line of sharp contrast of intensity. To avoid perturbations on the interface, we preferred using an exploded optical setup made of an objective placed at about its focal distance (30 mm) from the sample and a digital camera capturing the observed part of the field on a matrix of 1024×768 pixels. In practice, this turned about visualizing a 400 μm part of interface, i.e., about three dendrites, with an optical resolution of 0.5 μm per pixel. The frequency of video recording was adjusted so as to provide at least a dozen of images per branching period and the total observation time was taken so as to allow the observation of about 10^3 sidebranch emissions. For instance, at a velocity of $V = 15$ μm s^{-1} where the mean sidebranching period is $T_S = 4.2$ s, this called for a sampling frequency of three images per second and a total observation time of more than 1 h.

B. Sidebranching signal and correlation analyses

Above a critical velocity $V_c = 1.7$ μm s^{-1}, the initial planar interface destabilizes into an array of cells [Fig. 3(a)]. Increasing further the velocity, cells emit sidebranches and are renamed dendrites [Figs. 3(b)–3(d)]. This phenomenon is the result of a sidebranching instability which is supercritical with respect to the sidebranch amplitude. It arises above a critical velocity $V_S(\Lambda)$ which varies between 8 and 15 μm s^{-1} depending on the dendrite spacing Λ [21]. The sidebranch amplitude starts from zero at the sidebranching onset [Fig. 3(b)] and then grows continuously with both the velocity and the dendrite spacing. At moderate velocities, sidebranching appears by bursts separated by short quiet periods [Fig. 3(c)]. This corresponds to a moderate sidebranching regime. However, as velocity increases, the periods with no sidebranching shrink and the bursts eventually overlap [Fig. 3(d)]. One then arrives to the strong dendritic regime. Sidebranching will be analyzed here in both kinds of regimes.

Information on sidebranching is obtained from the successive intersections of the solidification interface with a line placed at a given distance z_0 from the dendrite tip [Fig. 4(a)]. The successive abscissa $x(z_0,t)$ recorded over the time provides a one-dimensional signal [Fig. 4(b)] which reflects the sidebranching dynamics. In the moderate sidebranching regime, it typically spreads over 1 h with a sampling time of 1/3 s, i.e., over about 10^3 sidebranch emissions of period $T_S \approx 4$ s, each sampled about 12 times. Its amplitude is several microns with a typical resolution of 0.5 μm per pixel, thus resulting in interface fluctuations over more than 20 pixels on the cutting line. Similar or better spatial and dynamical resolutions are obtained on any dendrite and in either the moderate or strong dendritic sidebranching regime possibly by increasing the sampling rate if required.

Two different, albeit related, methods are used to analyze the sidebranching signals. Both aim at evaluating the correlations between two centered signals $s_1(t)$ and $s_2(t)$ for a running delay τ between both. The signals addressed could be the actual sidebranching signals or their envelopes. The first method, based on correlation functions, provides an in-

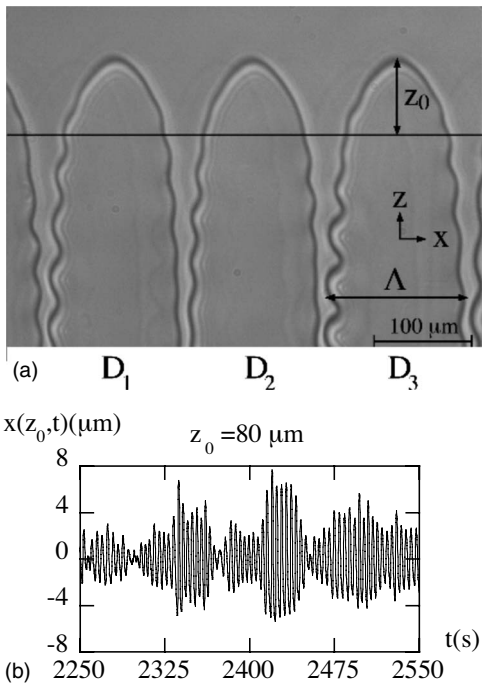

FIG. 4. Dendrites in the moderate sidebranching regime. $V = 15$ μm s^{-1} (a) Array of dendrites showing moderately developed sidebranches. Extracted signals correspond to the successive intersections of the x axis with the interface as time proceeds. They are taken at a distance $z_0 = 80$ μm from the dendrite tip. (b) Sidebranching signal showing vanishing periods of sidebranch amplitude. It has been extracted from the left side of dendrite D_1.

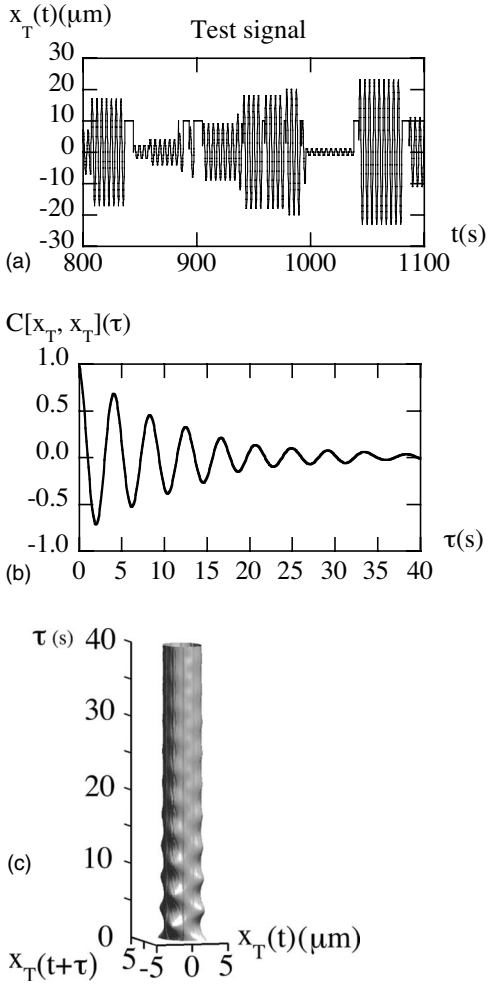

FIG. 5. Test signal and correlation analyses. (a) Test signal $x_T(t)$ made by juxtaposition of sinusoidal bursts involving equally distributed random lengths, amplitudes, and phases mimicking those displayed by sidebranching signals. (b) Autocorrelation function. (c) Isodensity surface in the phase space $\{x_T(t), x_T(t+\tau), \tau\}$.

tegral measure of the overlaps of the delayed centered signals $s_1(t)$, $s_2(t+\tau)$. The second method, based on phase space reconstruction, addresses the trajectory made by the successive points $[s_1(t), s_2(t+\tau)]$ as time proceeds. It provides this way a picture in phase space whose structure and evolution with τ reveal correlations.

After being detailed below, both methods will be further exemplified and compared on a test signal $x_T(t)$ built so as to mimic sidebranching signals (Fig. 5). This signal is made by juxtaposing sinusoidal bursts with random lengths, amplitudes, and phases. In particular, the number N of periods in a burst, the burst amplitude A, and the phase difference φ with the preceding burst follows a uniform distribution within the following ranges: $1 < N < 12$, relative amplitude range $A_{\max}/A_{\min}=5$, and $0.1 \leq \varphi/2\pi \leq 0.9$. Here, the phase shifts are provided by suitable rest periods and are only considered beyond $\varphi=0.1 \pmod{2\pi}$ so as to correspond to an actual burst. The periods of the sinusoids are equal to the sidebranching period $T_S=4.2$ s of the signal extracted in Fig. 4 and the sampling time is 1460 s.

We thus consider a couple of centered signals $s_1(t)$, $s_2(t)$, defined on the same time length T. The normalized correlation function $C[s_1,s_2](\tau)$ of these signals is given by the following integrals, τ denoting a running delay:

$$C[s_1,s_2](\tau) = c_{1,2}(\tau)/[c_{1,1}(\tau)c_{2,2}(\tau)]^{1/2}, \tag{1}$$

$$c_{i,j}(\tau) = \int_0^{T-\tau} \tilde{s}_i(t)\tilde{s}_j(t)dt, \tag{2}$$

$$\tilde{s}_1(t) = s_1(t), \quad \tilde{s}_2(t) = s_2(t+\tau). \tag{3}$$

Here $\tilde{s}_i(t)$ takes account of the delay τ of signal 2 with respect to signal 1. At each delay τ, the integrals $c_{i,j}(\tau)$ appear as a scalar product in the signal space. In particular, $c_{1,1}(\tau)^{1/2}$ and $c_{2,2}(\tau)^{1/2}$ correspond to the magnitude of signals 1 and 2 and $C[s_1,s_2](\tau)$ to their normalized scalar product: $-1 \leq C \leq 1$. A perfect correlation then refers to $C=1$, a perfect anticorrelation to $C=-1$ and an absence of correlation to $C=0$.

The integrals are computed on the finite intervals $T-\tau$ over which the signals overlap. Here, the delays τ are considered not larger than 60 s, i.e., the duration of 15 sidebranchings in the moderate sidebranching regime. When T refers to the total signal length (about 1 h), the reduction in the overlap length with increasing delays can be neglected. However, when the signal is restricted to a burst, T reduces to about 50 s so that the overlap length may vanish at large τ. For τ too close to T, this eventually makes the number of data points $N(\tau)$ of the integrals insufficient to establish a well-defined statistics. In practice, as the relative dispersion of data corresponds to $N(\tau)^{-1/2}$, computed integrals remain meaningful until $N(\tau) \approx 25$, i.e., with the selected sampling times of at most $T_S/12$, until $T-\tau$ about two sidebranchings or less.

When applied to sidebranching signals, the normalized correlation function $C[s_1,s_2](\tau)$ will be found to oscillate at the mean sidebranching period T_S. This simply reflects the fact that increasing the delay τ by $T_S/2$ mainly makes the signal $\tilde{s}_2$ reverse sign. The interesting feature will then stand more in the amplitude of the correlation function than in its oscillation and, especially, in its distance to the criteria for perfect correlation ($C=1$) or no correlation ($C=0$). In particular, for autocorrelations, i.e., for $s_2=s_1$, it will appear that the amplitude of C starts from 1 by definition ($\tilde{s}_2=\tilde{s}_1$ for $\tau=0$) but shrinks to zero on a characteristic delay τ_c which provides an intrinsic coherence time of the signal [e.g., Fig. 5(b)]. More generally, both autocorrelation and cross-correlation functions will be considered to clarify the coherence of the sidebranching signals emitted by one or several dendrites.

The alternate method for revealing signal correlations addresses the trajectories made, for given running delays τ, by the successive points $[s(t), s(t+\tau)]$ of a centered signal $s(t)$ as time proceeds. It provides a picture whose normalized density corresponds to the probability density function (pdf) $p(x,y)$ of finding given values of $s(t)=x$ and $s(t+\tau)=y$, i.e., given points of coordinates (x,y) in the phase plane [e.g., Fig. 5(c)].

If the signals $s(t)$ and $s(t+\tau)$ are perfectly uncorrelated, the pdf $p(x,y)$ splits into two separates pdf: $p(x,y)=p_1(x)p_2(y)$ with $p_1=p_2$ since the two signals are simply delayed. The density picture is then symmetric with respect to the bissectrices. In addition, as the pdf $p_1=p_2$ decreases with the distance to 0, the density picture displays a faint cross aligned with the x and y axes.

On the opposite, if the signals $s(t)$ and $s(t+\tau)$ are perfectly correlated, they yield a density picture aligned with the first bissectrix when in phase, invariant by rotation when in phase quadrature, and aligned with the second bissectrix when in phase opposition. In addition, varying τ is expected to have no effect on uncorrelated signals but to change the phase shift of correlated signals. Therefore, the density pictures drawn when plotting the points $[s(t),s(t+\tau),\tau]$ in a three-dimensional space (x,y,τ) should reveal autocorrelation by an alternance between pictures concentrated along circles or one or the other bissectrix. However, as τ increases, loss of correlation should reduce these features to eventually yield a density picture mainly independent of τ.

In a sense, this method corresponds to looking for recovering Lissajoux-type figures from coherent signals. As it provides an accumulated density of points, it is less sensitive to phase jumps or phase disagreements. In particular, such kinds of perturbations cannot prevent the main symmetries of the density picture to emerge whereas they should lower the value of correlation functions, hence obscuring the evidence of correlations. In practice, visualization of the density picture will be obtained by extracting an isodensity surface in the (x,y,τ) space [e.g., Fig. 5(c)].

The connection between both methods is obtained by considering the moment of inertia $I(\tau)$ with respect to the first bissectrix of the normalized density picture $p(x,y,\tau)$ made by the successive points $[s(t),s(t+\tau)]$. It writes

$$I(\tau)=\int p(x,y,\tau)\frac{(x-y)^2}{2}dxdy \tag{4}$$

with

$$\int p(x,y,\tau)x^2dxdy=c_{1,1}(\tau)/N(\tau),$$

$$\int p(x,y,\tau)y^2dxdy=c_{2,2}(\tau)/N(\tau), \tag{5}$$

where $N(\tau)$ is the total number of points considered. Noticing that $c_{1,1}(\tau)=c_{2,2}(\tau)$ since the two signals are simply delayed one with respect to the other and that $\int p(x,y,\tau)xy\ dxdy=c_{1,2}(\tau)/N$, one then obtains $I(\tau)=[c_{1,1}(\tau)-c_{1,2}(\tau)]/N(\tau)$ and, finally,

$$I(\tau)=\frac{c_{1,1}(\tau)}{N(\tau)}[1-C(s,s)(\tau)]. \tag{6}$$

The moment of inertia $I(\tau)$ thus appears simply proportional to the anticorrelation function $(1-C)$. In particular, if for the delay τ, the signals are in phase, $C=1$, the corresponding points are aligned on the first bissectrix and $I=0$. On the opposite, if the signals are in phase opposition, $C=-1$, the corresponding points are aligned on the second bissectrix and I is maximal. This link between I and C shows that autocorrelation functions actually correspond to an integral feature of the density picture. This stresses that more information are contained in the latter than in the former.

The analyses of the test signal are displayed in Figs. 5(b) and 5(c) according to both methods. In both of them, the coherence time is evidenced by the delay required to converge to uniformity, i.e., $C=0$ [Fig. 5(b)] or to a τ-invariant density picture [Fig. 5(c)]. One finds $\tau_c\approx 25$ s, i.e., with $T_S=4.2$ s, $\tau_c\approx 6T_S$, i.e., six sidebranches. This is actually coherent with uncorrelated bursts varying in lengths between 1 and 12 sidebranches, as considered in the test signal.

IV. GLOBAL ANALYSIS OF THE DENDRITIC SIGNAL

We address the main features displayed by sidebranching signals. Attention will be focused here on the moderate sidebranching regime, the analysis of the strong sidebranching regime being postponed to Sec. VIII. In particular, quantitative illustrations will be obtained from an arbitrary reference signal representative of sidebranch correlations in the moderate sidebranching regime. This signal, a part of which is displayed in Fig. 4(b), has been extracted over a sampling period of 3585 s from the left side of the dendrite D_1 of Fig. 4(a). It refers to the variables $G=78$ K cm^{-1}, $V=15$ μm s^{-1}, $\Lambda=150$ μm, and $z_0=80$ μm and will be used in the following except when explicitly stated.

A. Sidebranches and bursts

As noticeable with the naked eye [Fig. 4(b)], sidebranching signals display oscillations related to sidebranch emissions, but grouped by packs of about four to ten sidebranches. We shall call bursts these sidebranch packs.

The periods T_S between consecutive sidebranch emissions are mostly independent of the dendrite size Λ [Fig. 6(a)]. It, however, decreases with the pulling velocity V from about 6 s to 1 s in our velocity range [Fig. 6(b)]. As found in a previous study [21], the sidebranching period varies as a power law of V with an exponent close to $-3/2$: $T_S\propto V^{-1.6}$.

While the tip advances by $z_0=80$ μm, the sidebranches develop and reach an amplitude of ± 4 μm on the cutting line of the reference signal [Fig. 4(b)]. This indicates that the fluctuations of normal velocity which yield sidebranch formation are of the order of ± 4 $V/80$ here, i.e., ± 0.75 μm/s for $V=15$ μm/s. This corresponds to a moderate velocity for interface dynamics, of the order of the critical velocity V_c. However, it appears from Fig. 4(a) that the two first noticeable interface bumps starting from the tip on a dendrite side display a factor 2 in amplitude. This shows that sidebranching, nevertheless, corresponds to a large amplification at the scale of sidebranches.

On the reference signal, one notices some depletions of the signal amplitude [Fig. 4(b)]. They make a natural separation between sidebranch bursts following which they may be identified unambiguously. In particular, in each of them, the sidebranch amplitude is found to rise, saturate, shrink, and eventually vanish. We, nevertheless, stress that these features are prone to the moderate sidebranching regime. Be-

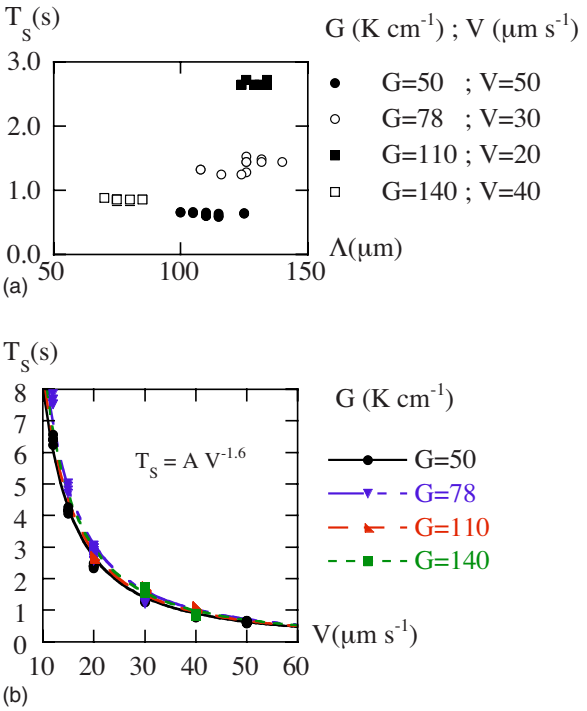

FIG. 6. (Color online) Evolution of the sidebranch frequency with the dendrite spacing Λ (a) or the growing velocity V (b). In (b), a power law $T_S(V)$ is fitted to the data: $T_S=AV^{-1.6}$ with $A=325$, 373, 344, and 360 in the figure units for $G=50$, 78, 110, and 140 K cm^{-1}.

yond, in the strong sidebranching regime, bursts are found to overlap, thus calling for a different analysis postponed to Sec. VIII.

The bursts within which sidebranches are emitted display irregular lengths T_B ranging from about 4 to 26 sidebranches. The typical frequency of burst occurrence as a function of their lengths is shown in Fig. 7 for the reference signal. One observes a peak of occurrence for $T_B=6T_S$ with a standard deviation of $4.5T_S$, a mean of $8T_S$ and a regular decrease up to $T_B\approx 26T_S$.

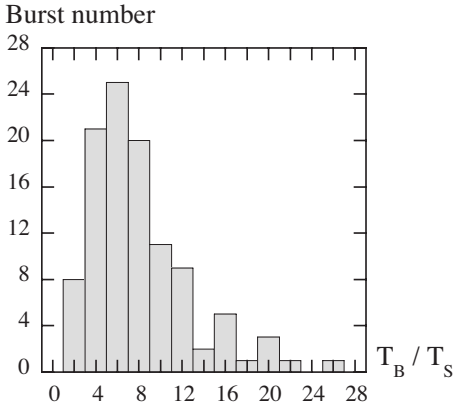

FIG. 7. Histogram of the burst lengths T_B in the reference signal. The sidebranching period T_S is taken as the time unit.

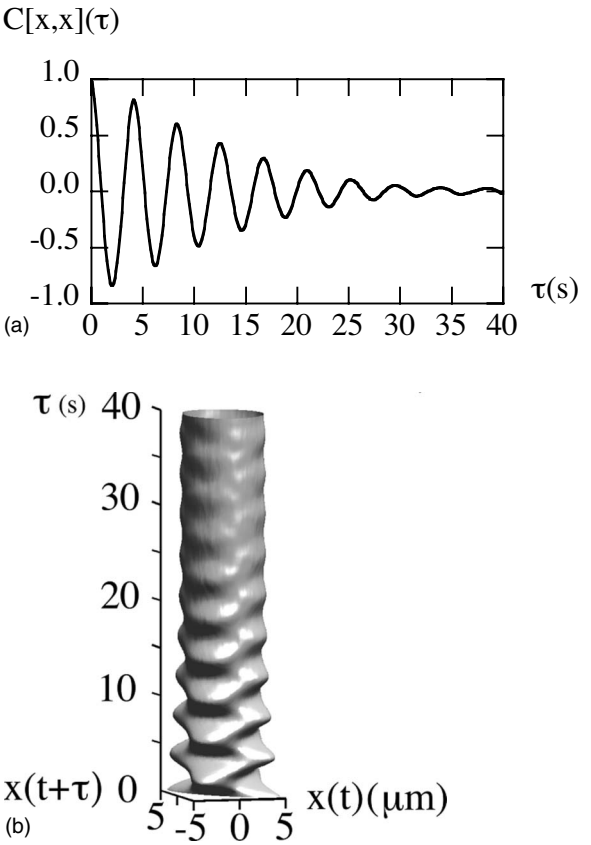

FIG. 8. Autocorrelation of the whole dendritic signal. (a) Autocorrelation function of the signal. The decay over an unexpectedly long period of 30 s, i.e., about seven sidebranching periods, points to some coherence in the signal. (b) Isodensity surface of the sidebranching signal in the phase space $\{x(t),x(t+\tau),\tau\}$. The repetitive symmetries of the surface with respect to the bissectrix of the plane $\{x(t),x(t+\tau)\}$ reveal the signal coherence.

B. Autocorrelation of a dendritic signal

Figure 8(a) displays the autocorrelation function $C[x,x](\tau)$ of the reference signal. As expected, it shows oscillations at the sidebranching period T_S starting from $C=1$ at $\tau=0$ s. However, the amplitude of the oscillations regularly decreases with the time delay until reaching a faint asymptotic value. We define the coherence time τ_c of the signal as the delay τ required for reaching this asymptotic value.

Interestingly, the coherence time reaches a surprisingly large value $\tau_c\approx 7T_S$, i.e., 30 s, which corresponds to a noticeable growth distance of $V\tau_c\approx 440$ μm for the dendrite tip. Such a large correlation over time and space reveals an unexpected order in the sidebranching signal. This is confirmed by addressing the reconstruction of the signal attractor in phase space. Figure 8(b) then shows in the phase planes $\{x(z_0,t),x(z_0,t+\tau),\tau\}$ an alternance of concentration around the first bissectrix, a circle and the second bissectrix, up to roughly $\tau\approx 30$ s. This corresponds to an alternance of phase agreement, phase quadrature, and phase opposition between signals which stands as a signature of signal coherence over a finite coherence time $\tau_c\approx 30$ s.

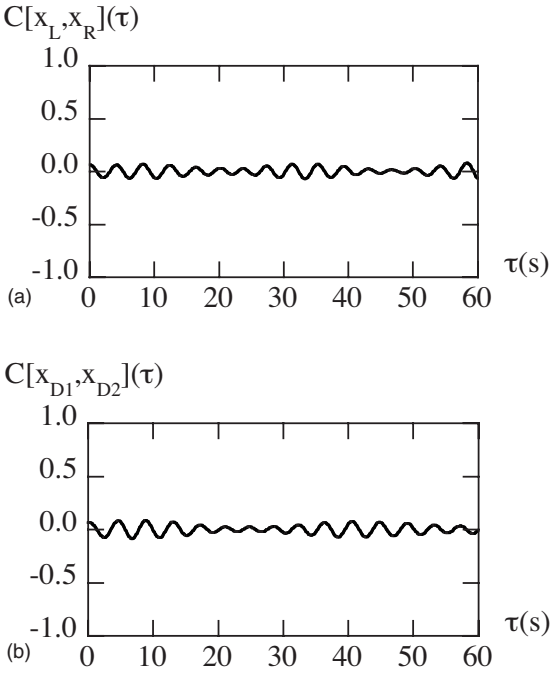

FIG. 9. Cross-correlation functions of dendritic signals extracted from the left and right sides of the same dendrite (a) or from different dendrites (b). Signals are extracted from dendrite D_1 in (a) and from the left sides of dendrites D_1, D_2 in (b) [see Fig. 4(a)].

C. Cross-correlation of the dendritic signal

Following the evidence of internal coherence in dendritic signals, it appears relevant to address their cross-correlation function. For this, we consider the dendritic signals obtained at the same distance $z_0=80$ μm from the tips on the left and right sides of the same dendrite, actually the dendrite labeled D_1 in Fig. 4(a). We call $x_L(z_0,t)$ and $x_R(z_0,t)$ the corresponding signals captured over a sampling time of 3585 s. Their cross-correlation function, reported in Fig. 9(a), displays some oscillations linked to sidebranch emissions. However, for any delay τ, its amplitude never emerges above the noisy background around $C=0$. This feature, which differs from that displayed in free growth [8], indicates an absence of correlation between the two signals here.

The same conclusion is reached for other z_0 and for pairs of signals belonging to different dendrites. In particular, Fig. 9(b) reveals an absence of correlation between signals extracted from the left sides of dendrites D_1 and D_2.

D. Conditional analysis of signal correlation

As sidebranches are emitted by bursts, it appears relevant to address the link between sidebranch coherence and burst length. For this, we perform a conditional analysis of signal correlations with respect to burst lengths by considering three families of bursts: those smaller than $6T_S$ (heavy black signal on Fig. 10), those in between 6 and $12T_S$ (light blue signal on Fig. 10), and those above $12T_S$ (faint red signal on Fig. 10). We obtain, respectively, $\tau_c=4T_S$, $6T_S$, and $10T_S$, showing an increase in the mean coherence time with the burst lengths. This observation stresses the importance of bursts for sidebranch coherence and calls for considering them for further analysis of sidebranch correlations.

E. Separate time scales

Sidebranching signals thus involve two kinds of phenomena at two different time scales: the emission of sidebranches on a short time scale, the sidebranching period T_S, and the occurrence of sidebranch bursts on a larger time scale, the burst length T_B. Whereas the sidebranching period T_S appears nearly constant along the entire signal, the burst length T_B varies in between 4 to $26T_S$ with a mean at $8T_S$. This points to a definite separation of time scales between sidebranching and bursts.

To further analyze sidebranch correlations, it thus appears relevant to consider separately these two times scales on the sidebranching signal. This turns out analyzing the sidebranching signal $s(t)=x(z_0,t)$ in amplitude $a(t)$ and phase $p(t)$: $s(t)=a(t)p(t)$. Here, the amplitude $a(t)$ is defined positive and $p(t)$ oscillates in between $[-1,1]$. Then, $a(t)$ represents the envelope of the signal $s(t)$ and displays a scale of variation equal to the mean burst length $\langle T_B\rangle$. On the other hand, $p(t)$ stands for the phase of the signal whose scale of variation is the sidebranching period T_S. The coherence of the whole signal $s(t)$ thus requires that of the phase signal $p(t)$ but also depends on the features of the amplitude signal $a(t)$.

In practice, the amplitude signal $a(t)$ may be obtained at a sufficient accuracy by interpolation between the signal

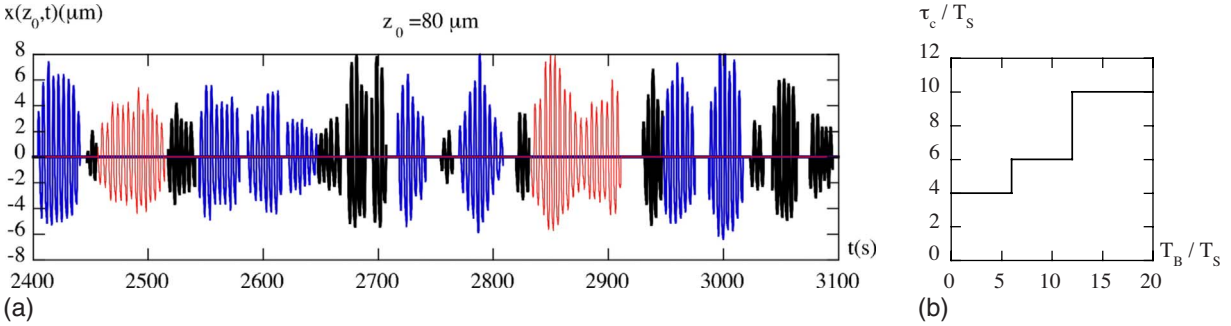

FIG. 10. (Color online) Conditional analysis of signal correlation with respect to burst length. (a) Signal analysis. Colors and thicknesses refer to different classes of burst length T_B: $T_B<6T_S$ (heavy black), $6T_S<T_B<12T_S$ (light blue), and $12T_S<T_B$ (faint red). Autocorrelation functions are considered by extracting each of these burst classes. (b) Evolution of the coherence time τ_c with the burst length T_B on the three ranges.

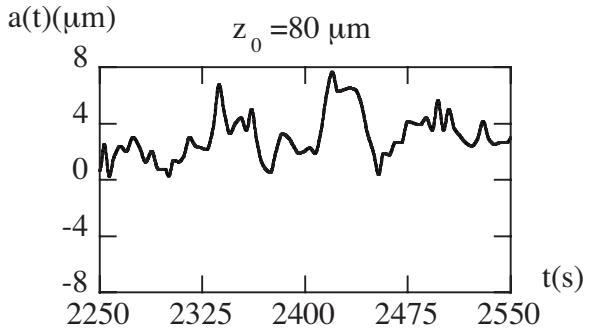

FIG. 11. Amplitude signal corresponding to the sidebranching signal of Fig. 4(b). It is obtained by interpolation between successive maxima.

maxima. For the reference signal of Fig. 4(b), one then obtains the graph displayed in Fig. 11. Here the differences with the actual signal envelope stand at the time scale T_S which is small compared to the signal time scale T_B. They will thus be of negligible influence on the analysis of the coherence of the amplitude signal.

In principle, the phase signal should then be deduced from $s(t)$ and $a(t)$ as the ratio $p(t)=s(t)/a(t)$. This procedure should be adequate for studying the phase coherence in the domains where $a(t)$ varies slowly as compared to the phase signal, i.e., where the separation of time scales is effective. However, in the domains where $a(t)$ quickly grows or shrinks, i.e., at the beginning or the end of bursts, the actual variation scales of $a(t)$ and $p(t)$ are similar and the decomposition in amplitude and phase becomes ambiguous and sensitive to the zero level defined for the signal. For this reason, we prefer to keep analyzing below the phase coherence from the whole signal $s(t)$.

The next two sections are devoted to clarify the coherence in phase and amplitude of the sidebranching signals by addressing the correlations of sidebranch occurrences in bursts (Sec. V) and those of burst occurrences in the whole signals (Sec. VI).

V. COHERENCE OF DENDRITIC SIDEBRANCHING INSIDE A BURST

We focus attention here to the internal coherence of sidebranching in a burst. For this, we address autocorrelation and cross-correlation functions from signals coming from different locations and different dendrites.

A. Autocorrelation of a sidebranching burst

Figure 12(a) displays a typical autocorrelation function of a sidebranching burst. It is obtained from a burst of the reference signal, hereafter called b, and referring to the range 2409 s$<t<$2451 s in Fig. 4(b). The puzzling thing, which provides a main outcome of the study, is the large and nearly constant amplitude of this correlation function. Starting by construction from $C=1$ at $t=0$, its maxima remain above 0.8 for all delays τ until the burst end, $\tau \approx 10T_S$. This result, which appeared on all bursts, demonstrates a large correlation of sidebranches in a burst and thus a large level of sidebranching coherence within each burst.

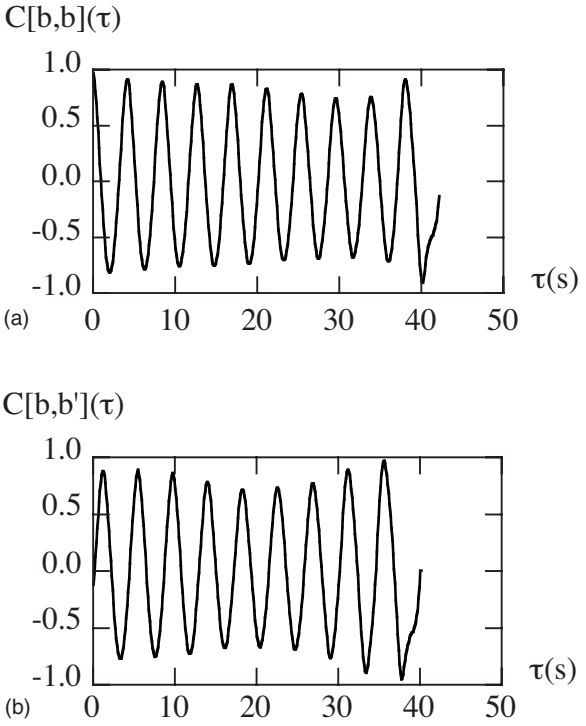

FIG. 12. Correlation functions of bursts belonging to the same sidebranching signal, here the signal extracted from the dendrite D_1 of Fig. 4. (a) Autocorrelation function of a single burst b. (b) Cross-correlation function of two bursts b and b'.

B. Cross-correlation of sidebranching bursts coming from the same signal

Following the intrinsic coherence of sidebranching in a burst, it appears judicious to address the cross-correlation between sidebranching bursts extracted from the same dendritic signal. Figure 12(b) shows a typical graph obtained from the above burst b and another burst b' extracted at 2772 s$<t<$2812 s in the same reference signal. Here too, the correlation function $C(\tau)$ keeps a surprisingly large amplitude, above 0.8 for all delays τ until the end of the bursts overlap: $\tau \approx 10T_S$. Its value $C(0)$ refers to the mismatch between the sidebranching phases of the two bursts. However, the origin taken for delays being arbitrary, it has no specific signification for the signal coherence. On the other hand, the large value of the correlation function for all delays indicates a relative variation in the sidebranching frequency below $T_S/T_B \approx 10^{-1}$ in each burst, and thus its large stability in both of them. Similarly, the absence of beating in the cross-correlation function indicates a relative difference between the sidebranch frequencies of bursts smaller than $T_S/2T_B \approx 5\times 10^{-2}$ and thus their large closeness. Similar conclusions were obtained on other couple of bursts extracted from the same signal.

C. Cross-correlation of sidebranching bursts coming from different signals

We now extend the cross-correlation studies by considering sidebranching signals extracted still at the same distance

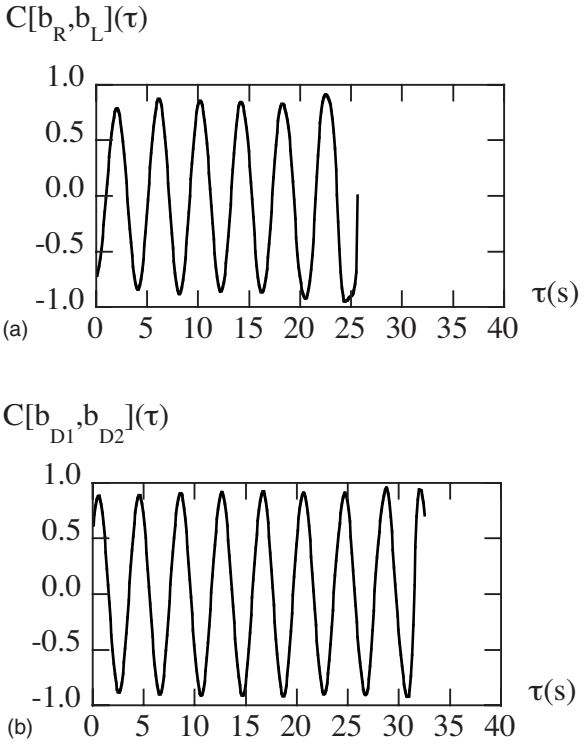

FIG. 13. Cross-correlation functions of bursts extracted from different sidebranching signals. (a) Bursts b_R and b_L emitted on the right side and the left side of the same dendrite, the dendrite D_1 of Fig. 4(a). (b) Bursts b_{D1} and b_{D2} emitted on two different dendrites, the left side of the dendrite D_1 and the right side of the dendrite D_2 of Fig. 4(a).

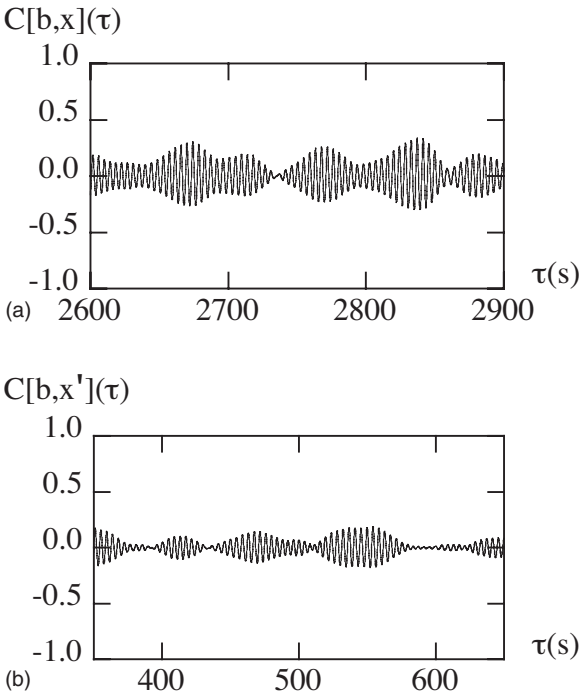

FIG. 14. Cross-correlation functions between a burst and a sidebranching signal emitted on the same dendrite (a) or on different dendrites (b). The persistence of large amplitudes at large delays evidences the coherence of sidebranching in each burst. Jumps of the sidebranching phase between bursts are noticeable from phase mismatches in the oscillations of the cross-correlation functions. The burst signal is the burst b extracted from dendrite D_1 and defined in Sec. V A. (a) The sidebranching signal is the reference signal $x(t)$ extracted from the same dendrite. (b) The sidebranching signal $x'(t)$ is extracted from the dendrite D_2.

$z_0=80$ μm from the dendrite tips but on different dendrites or different dendrite sides.

1. Left and right sides of a dendrite

Figure 13(a) shows the cross-correlation function $C(\tau)$ between two bursts extracted at the same time from the same dendrite, one b_L from the left side of dendrite D_1 of Fig. 4(a) (actually the above burst b) and the other b_R from its right side. At zero delay τ, it appears that sidebranches are not synchronized since the value $C(0)$ is lower than unity. However, a large amplitude of cross-correlation is noticeable, despite the change in dendrite sides between the two signals. This is at variance with the absence of cross-correlation found for signals extended over many bursts [Fig. 9(a)]. In comparison, the large correlation evidenced here stresses the internal coherence of each burst and the closeness of their frequency. However, the sidebranching phase, as well as the burst occurrence, shows no synchronization from one to the other side of the dendrite, despite them being emitted on the same dendrite.

2. Different dendrites

Figure 13(b) displays the cross-correlation function obtained by taking a couple of bursts b_{D1}, b_{D2} extracted from two different dendrites, the left side of dendrite D_1 and the right side of dendrite D_2 of Fig. 4(a). Here too, the cross-correlation function keeps a large amplitude for all delays, in contrast with the absence of correlation found on signals extended over many bursts [Fig. 9(b)]. This stresses the robustness of coherence among the whole interface, whatever the dendrite, as well as the stability and the closeness of sidebranch frequencies on the solidification front.

D. Long-time cross-correlation of a burst with a signal

As the above large amplitudes of cross-correlation functions trace back to the intrinsic coherence of sidebranching in a burst, they should persist when confronting a burst with a series of burst, i.e., when considering the cross-correlation of a burst with a dendritic signal. This is achieved here by performing the cross-correlation of burst b with the reference signal from which it has been extracted. The correlation function $C(\tau)$, shown in Fig. 14(a), exhibits a large amplitude for any delays τ, thus evidencing sidebranching coherence. It also shows amplitude modulations over a mean burst length separated by periods of zero correlation that are significantly longer than in the actual signals [Fig. 4(b)]. They thus result not from amplitude modulations but from the variable phase shifts between successive bursts. Following them, no net correlation may appear when the burst b equally overlaps two parts of neighbor bursts.

Both results highlight the large coherence of sidebranching in each burst, the stability of the sidebranching frequency, and the phase uncorrelation of sidebranching from burst to burst. In particular, the latter feature explains the compatibility between the long-time correlation between the burst b and the whole signal and the rapid decay of the signal autocorrelation function [Fig. 8(a)]: for delays τ larger than about a burst length, the autocorrelation function $C(\tau)$ results from the sum of the cross-correlations between various bursts of the signal; their phase uncorrelation then yields a net zero integral contribution, $C=0$.

Similar observations are made when performing the cross-correlation of the burst b with the signal emitted from another dendrite, here the left side of dendrite D_2 [Fig. 14(b)]. This confirms the coherence of sidebranching in bursts and the closeness of their sidebranching frequency, independently of the dendrite considered.

VI. UNCOHERENCE OF BURST EMISSIONS IN THE SIDEBRANCHING SIGNAL

We now focus attention on the coherence of burst emissions by investigating the auto- and cross-correlations involved in the envelope $a(t)$ of the sidebranching signal. As shown by comparison between Figs. 4(b) and 11, this envelope actually skips sidebranching but conveys burst emissions. It is thus suitable for analyzing their coherence. However, to facilitate the interpretation of correlation functions, it will appear more convenient to use centered envelopes $\tilde{a}(t)$ in the following.

A. Autocorrelation of an amplitude signal

Figure 15(a) shows the autocorrelation function of the centered amplitude $\tilde{a}(t)$ of the reference signal. It displays a decay to zero on a coherence time τ_a of about 33 s. Interestingly, this time appears quite close to the mean burst length $\langle T_B \rangle \approx 8T_S = 33.6$ s, meaning that the autocorrelation disappears as soon as a burst statistically overlaps its neighbor. This indicates the absence of long-range correlation in burst emissions, i.e., in both burst occurrences and burst lengths.

This conclusion is confirmed by considering an isodensity surface of the trajectory of the envelope signal in the phase space $\{a(t), a(t+\tau), \tau\}$. Figure 15(b) then shows, for short delays τ smaller than τ_a, a surface close to the first bissectrix as a result of the initial correlation of the signal with itself. However, for larger delays, it exhibits a nearly uniform surface showing none of the symmetries expected in case of correlations (Sec. III B). This, in particular, contrasts with the symmetric structures exhibited over several periods on similar surfaces for sidebranching signals [Fig. 8(b)]. Beyond the differences of time scales between sidebranching and bursts ($\langle T_B \rangle / T_S \approx 8$), this emphasizes the absence of correlation in the burst signal.

B. Cross-correlation of different amplitude signals

Despite the absence of temporal coherence in the amplitude signals, it appears relevant to investigate their spatial coherence by addressing the level of cross-correlations between signals belonging to different sides of a same dendrite or to different dendrites.

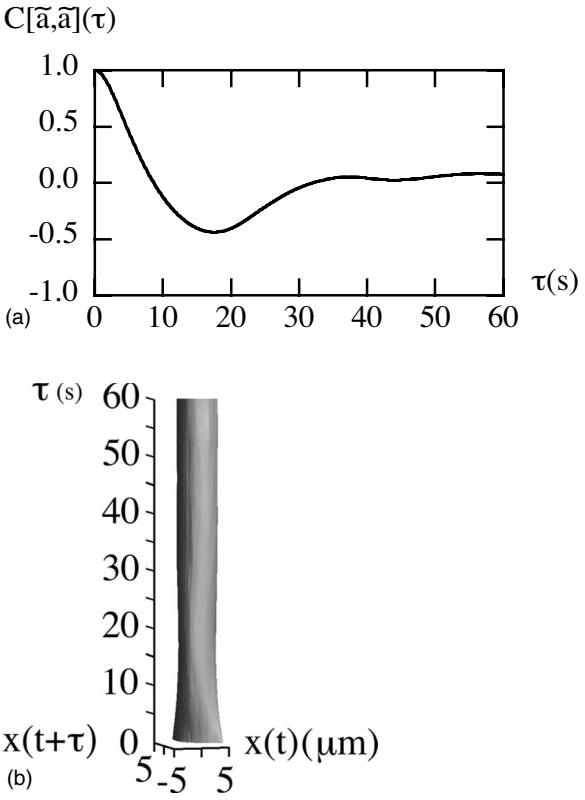

FIG. 15. Statistical analysis of bursts emitted in a sidebranching signal. (a) Autocorrelation function of the centered amplitude $\tilde{a}(t)$ of the reference signal. Its vanishing beyond 30 s, i.e., about a mean burst length, indicates an absence of correlation in burst emissions. (b) Isodensity surface of the amplitude signal in the phase space $\{a(t), a(t+\tau), \tau\}$. The absence of structure and of symmetries for τ larger than a mean burst length emphasizes the absence of coherence.

1. Left and right sides of a dendrite

We consider the centered amplitude of signals extracted on the left side $\tilde{a}_L(z,t)$ and the right side $\tilde{a}_R(z,t)$ of a dendrite. Their cross-correlation is shown in Fig. 16(a) for a representative dendrite, the dendrite D_1 of Fig. 4(a). It reveals no correlation, for any delay τ between the signals. In particular, even for zero delay, the level of correlation $C[\tilde{a}_L, \tilde{a}_R](0)$ is desperately low. This absence of correlation means that burst emissions on both sides of a dendrite are statistically independent one from the other.

2. Different dendrites

Signals referring to different dendrites are considered by addressing the centered amplitudes of the sidebranching signals extracted from the right side of dendrites D_1 and the left side of dendrite D_3 of Fig. 4(a). Here again, their cross-correlation function reported in Fig. 16(b) reveals no correlation for any delay τ between the signals, even for zero delay. This result, which echoes that found on the opposite sides of a dendrite, means the absence of any spatial coher-

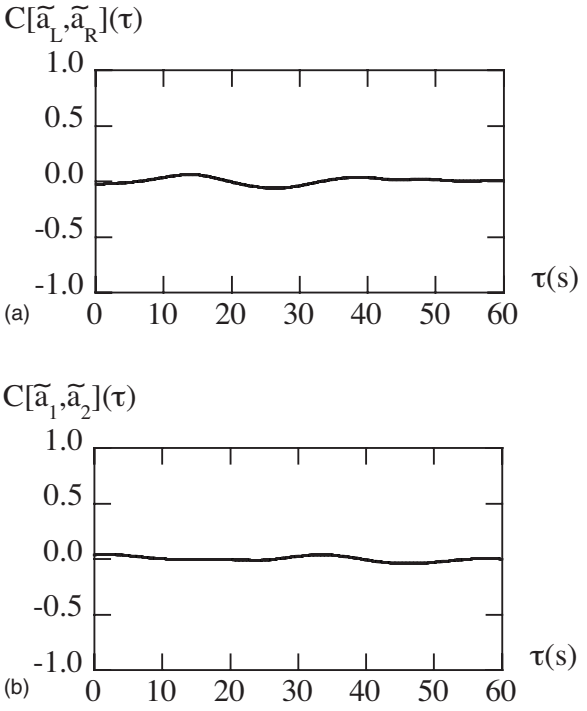

FIG. 16. Cross-correlation function of the centered amplitude of bursts belonging to different sidebranching signals. (a) Bursts emitted on the left side $\tilde{a}_L$ and the right side $\tilde{a}_R$ of the same dendrite, here the dendrite D_1 of Fig. 4(a). (b) Bursts $\tilde{a}_1$ and $\tilde{a}_2$ emitted on two different dendrites, here the right side of dendrites D_1 and the left side of dendrite D_3 of Fig. 4(a). Both show an absence of correlation.

ence in burst emissions. This, together with the above absence of temporal coherence, concludes to an absence of any kind of coherence in burst emissions on the dendritic interface.

VII. UNCORRELATION OF SIDEBRANCHING PHASES BETWEEN BURSTS

To complete the analysis of sidebranching coherence, it is worth addressing whether the sidebranching signal keeps the same phase when changing bursts or undergoes a phase jump.

A. Evidence of phase jumps between consecutive bursts

A phase jump between periodic functions involving the same period may be noticed by a marked decrease in their cross-correlation functions when the delay between signals is such that the first signal overlap half itself and half the second signal. This is apparent on the cross-correlation function $C(\tau)$ obtained from a couple of consecutive bursts b_1, b_2 extracted from the reference signal [Fig. 17(a)]. Figure 17(b) then shows large correlations at both small delays and large enough delays for making the first burst fully overlap the second. However, in between, its decrease below an amplitude of 0.5 reveals the existence of a phase mismatch between them.

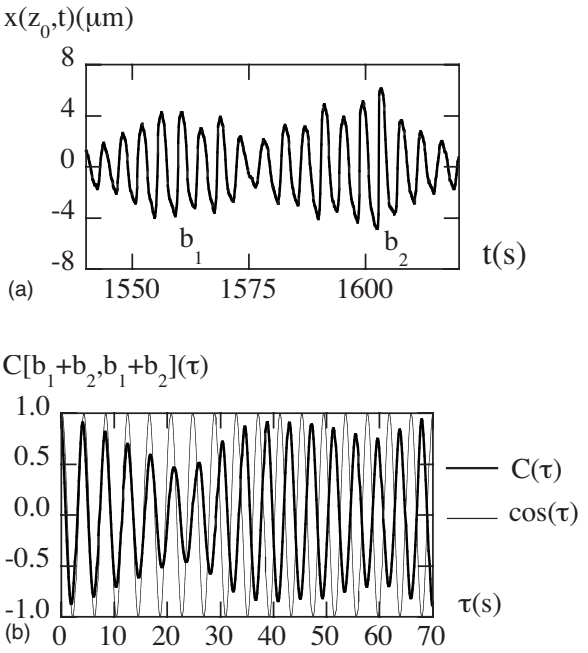

FIG. 17. Evidence of phase jumps between two neighbor bursts of the sidebranching signal. (a) Signal involving two neighbors bursts b_1 and b_2 taken from the reference signal of Fig. 4(b). (b) Autocorrelation function of the signal and comparison to a sinusoidal function with a period equal to the mean period of the first burst. A phase jump is noticeable at the transition between the two bursts.

The phase jump $\delta\varphi$ between bursts can also be directly detected on the phase of the cross-correlation function $C(\tau)$. Its maxima indeed occur at $\tau = nT_S$, $n \in \mathcal{N}$ for delays small enough for avoiding a large overlap between bursts and for $\tau = pT_S + \delta\varphi$, $p \in \mathcal{N}$ for delays so large that the first burst overlaps the second. The phase difference $\delta\varphi$ can be evidenced by superposing on the graph of the cross-correlation function $C(\tau)$ a sinusoidal function in phase agreement with it for small τ: its phase shift with $C(\tau)$ at large τ then evidences the phase jump $\delta\varphi$ [Fig. 17(b)].

B. Distribution of phase jumps between consecutive bursts

To address the phase jumps between consecutive bursts on the whole signal, we apply the above method to the whole bursts. We first identify each burst from a marked decrease of the signal amplitude [Fig. 10(a)]. We then adjust on each of them the phase of a sinusoidal signal at the sidebranching period so as to make the extrema of both signals simultaneous. The phase mismatch between the sinusoidal functions referring to consecutive bursts then gives the phase shift between bursts. Pixelization limits its accuracy to about one third of pixel, i.e., 10°.

Analysis of the reference signal reveals a distribution of phase jumps mainly uniform given the dispersion inherent to the limited number of data in each bin (Fig. 18). In particular, the median value of phase jumps is $\delta\varphi = \pi$ with a standard deviation of $\pi/2$, large enough for making the maximum of the histogram at $\delta\varphi = \pi$ not statistically significant. Accordingly, no correlation between neighbor bursts is evi-

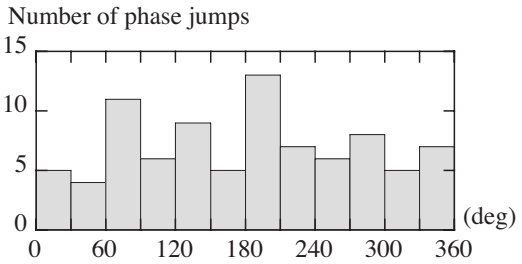

FIG. 18. Histogram of the phase jumps between consecutive bursts of the reference signal.

denced, even on a statistical viewpoint. Bursts are thus intrinsically coherent regarding the sidebranching signal but uncorrelated regarding both their occurrence and their sidebranching phase.

VIII. BEYOND THE MODERATE SIDEBRANCHING REGIME

We now extend the analysis of coherence to dendrites standing farther from the sidebranching onset and to asymmetric dendrites growing with an angle with respect to the thermal gradient. This will enable us to address the influence of sidebranch amplitude and of dendrite form on the sidebranching coherence.

A. Strong sidebranching regime

Figure 19(a) shows dendrites growing far from the sidebranching onset. All display well developed sidebranches from the tip vicinity down to the grooves with no rest part free of sidebranching. This questions the existence of sidebranch bursts here and the resulting implications on sidebranching coherence.

The early development of sidebranches makes them point toward a direction that is no longer normal to the dendrite axis **z**. As a result, the method for extracting sidebranching signals has to be adapted for ensuring a single intersection of the cutting line with the interface and avoid a spurious asymmetry between the rising and decreasing sides of a signal.

Figure 19(b) shows a part of a sidebranching signal extracted this way from the right side of dendrite D_2 of Fig. 19(a), at about 85 μm from the tip and along a cutting line inclined by 30° with respect to the dendrite axis. This signal, which extends over a sampling time of 160 s, will be taken hereafter as a reference signal and labeled $x(t)$.

This sidebranching signal displays oscillations at a small sidebranching period of $T_S=1.3$ s and a large amplitude of about 15 μm. As in the moderate sidebranching regime, it shows phase jumps in the vicinity of which the signal envelope abruptly shrinks to zero in a sidebranching period or less. It thus still seems to be made of bursts but which are no longer well separated as they were in the moderate sidebranching regime. Further correlation analyses are, nevertheless, required to confirm and clarify this qualitative analysis. They are reported below.

Following the continuous emission of sidebranches, the envelope signals are mostly constant, so that addressing their correlations appears useless here. We then turn attention to

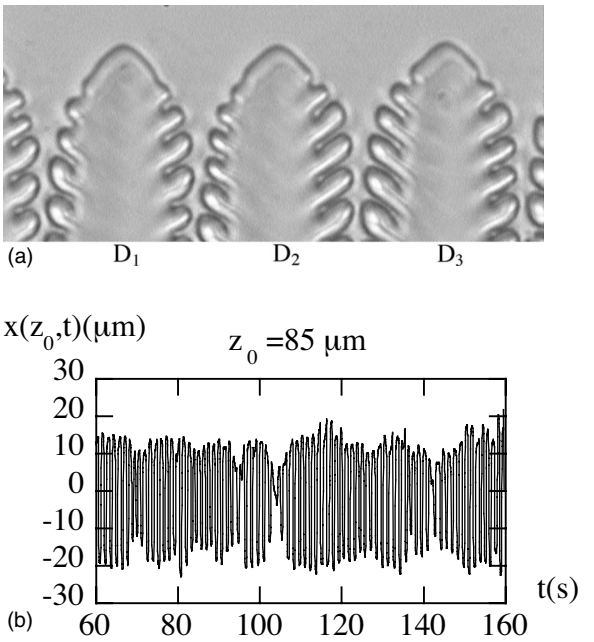

FIG. 19. Dendrites in the strong sidebranching regime. Thermal gradient, velocity, and dendrite spacing are $G=50$ K cm^{-1}, $V=30$ μm s^{-1}, and $\Lambda\approx 160$ μm. (a) Snapshot showing largely developed sidebranches close to the dendrite tips. (b) Sidebranching signal extracted on the right side of dendrite D_2 at a distance $z_0=85$ μm from its tip and along a cutting line normal to the mean interface. It involves oscillations at a small sidebranching period $T_S=1.3$ s and with a large amplitude of about 15 μm. Vanishing of the signal envelope is reduced to tiny periods of about one sidebranching. This signal will serve as a reference signal.

the correlations of the sidebranching signal. Figure 20 shows that its autocorrelation function exhibits oscillations at the sidebranching frequency, here $T_S=1.3$ s, bounded by an envelope decaying over a coherence time τ_c of several sidebranching periods $\tau_c\approx 6T_S$. This behavior is actually similar to that observed in the moderate sidebranching regime. The similarity between the two regimes also extends to the cross-correlation between signals extracted on different dendrites which, here too, show no correlation.

Further inquiry into the nature of sidebranching can be obtained by looking for the cross-correlation between a burst arbitrarily extracted from the reference signal and either the

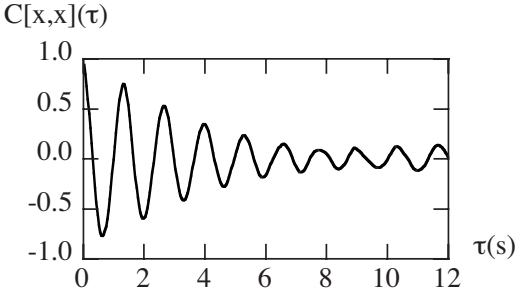

FIG. 20. Autocorrelation function of the reference signal. Its decay on $6T_S\approx 8$ s refers to the mean burst length beyond which phase jumps destroy the overall coherence of the sidebranching signal.

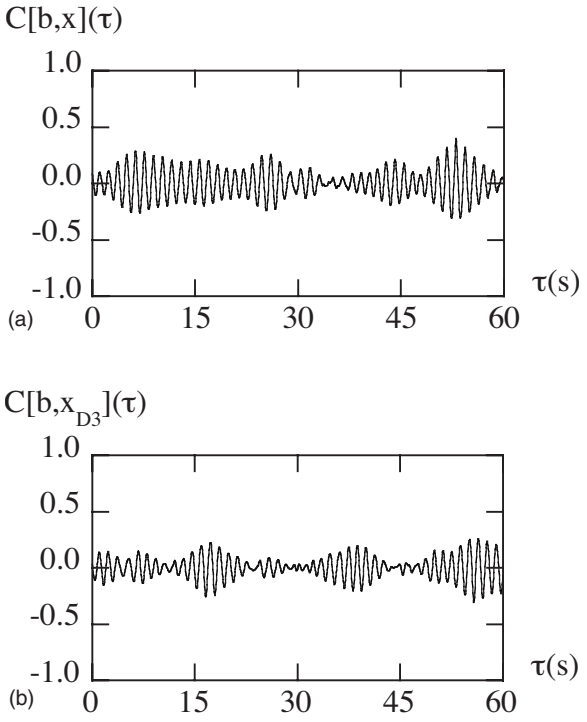

FIG. 21. Cross-correlation function between a burst and a sidebranching signal. The evidence of a large correlation amplitude well beyond the burst length shows the sidebranching coherence. Phase jumps are noticeable from the phase mismatches of the correlation function. (a) Same sidebranching signal as that of the burst (here, the reference signal). (b) Sidebranching signal referring to another dendrite (left side of dendrite D_3) than that of the burst (right side of dendrite D_2).

whole reference signal [Fig. 21(a)] or another signal referring to another dendrite (the left side of dendrite D_3) [Fig. 21(b)]. In both cases, repetitive bursts of coherence are obtained. They altogether reveal that sidebranching signals are made of a succession of coherent parts with variable phase relationships between them. Then, making a sidebranch burst glide on the signals yields successive periods of large correlations interrupted by the phase mismatch between the successive bursts. In particular, the important thing is that sidebranch bursts are still emitted here, even if this is no longer manifest from depressions of the sidebranch amplitude but by phase jumps.

The evolution of phase jumps during the drifting of sidebranches along the interface is reported in Fig. 22. Here, three signals have been extracted at three different distances z_0 from the dendrite tip on the right side of dendrite D_2. Their time origin is taken so that they refer to the same sidebranches. They all involve phase jumps that have been noticed with full lines. Interestingly, the lines referring to the same phase jump overlap, thus indicating that phase jumps have not evolved with respect to sidebranches. They were thus present until the very beginning of sidebranching and simply drifted together with the branches.

Interestingly, some phase jumps correspond near the dendrite tip to a depression of sidebranch amplitude. This is, for instance, apparent at $t=70$ s where the transition between bursts is noticeable at $z_0=36$ μm but much less visible at

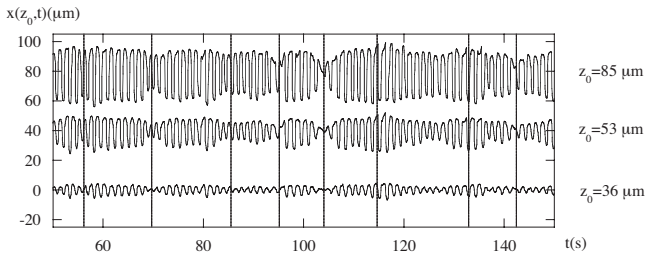

FIG. 22. Sidebranching signals taken on the same dendrite (D_2) and on the same (right) side but at different distances from the dendrite tip. Three values of z_0 have been considered: 36, 53, and 85 μm. The amplitude is found to increase by a factor 4 from the closest ($z_0=36$ μm) to the farthest ($z_0=85$ μm) point to the tip. The phase jumps detected at $z_0=85$ μm are indicated by thin lines. They are found at almost the same place at the other distances from the tip, $z_0=53$ and 36 μm.

$z_0=85$ μm. Although some other phase jumps do not apparently follow this rule (e.g., that occurring at $t=115$ s), this observation together with the conservation of phase jumps during sidebranch development provides a continuity between the two sidebranching regimes. In both of them, a raise of the sidebranch amplitude from zero may be associated with a burst; however, depending on the distance to the sidebranching onset it may be identified closer or farther from the tip. This conclusion means that the sidebranch amplitude plays here a secondary role, the primary role being held by the sidebranching phase. Alternatively, it stresses the physical equivalence between the moderate and strong sidebranching regime regarding the nature of sidebranching.

B. Asymmetric dendrites

Up to now, the principal axes of the cubic succinonitrile crystal were aligned with the sample depth direction, the thermal gradient **G**, and the isothermal lines. The crystal orientation thus matched the characteristic directions of the solidification setup so that a symmetric growth could be achieved. In particular, the growth direction of dendrites was parallel to **G** and their left and right sides showed similar sidebranch developments.

This configuration is, however, specific to laboratory experiments. In practice, the crystalline axes are usually misaligned with respect to the setup axes so that growth involves some asymmetry. To address this more generic case, we consider below the directional solidification of a crystal that is slightly misorientated with respect to the setup directions [56]. In particular, whereas one of its principal axes is still aligned with the sample depth, the two others involve a slight angle with respect to the thermal gradient and the isothermal lines. This results in asymmetric dendrites growing in a direction no longer parallel to **G** and showing different kinds of sidebranch dynamics on their sides. In particular, here, the right side of dendrites shows no branching whereas the left side involves some [Fig. 23(a)]. This, therefore, provides the opportunity of studying sidebranch developments without interactions with sidebranches emitted on the opposite side of the dendrite or on the facing groove of a neighbor dendrite.

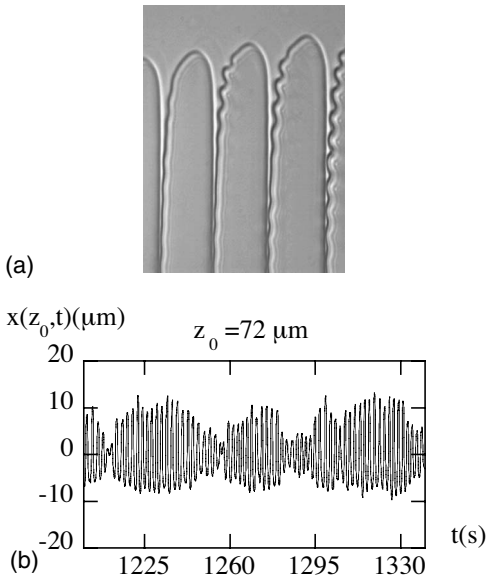

FIG. 23. Asymmetric dendrites. (a) Snapshot of asymmetric dendrites growing at an angle to the thermal gradient **G** following a misorientation of the crystal lattice. (b) Sidebranching signal extracted by intersection with a line normal to the mean interface.

Figure 23(a) shows dendrites referring to the following growth conditions: $G=140$ K cm^{-1}, $V=20$ μm s^{-1}, $\Lambda=101$ μm, Péclet number Pe$=1.47$, and an angle of 10° between a crystal axis and **G**. Following the dendrite misorientation, the dendritic signal is extracted by taking a cutting line making an angle of −27° with respect to the direction **G**. A representative part of the signal extracted this way over a sampling period of 1510 s at a distance $z_0 \approx 72$ μm from the tip is displayed in Fig. 23(b). It shows a sidebranching period of $T_S=2.15$ s and a sidebranch emission by bursts revealed by a depression of the signal envelope, as for symmetric dendrites (Sec. IV).

Correlations analyses of the sidebranching signals are reported in Fig. 24. As for symmetric dendrites, the autocorrelation of the sidebranching signal shows a decay over a coherence time $\tau_c \approx 5T_S$ [Fig. 24(a)]. Here too, its value is similar to both the mean burst length and the coherence time of the autocorrelation function of the signal envelope. It thus indicates a sidebranching coherence restricted to bursts. In contrast, the cross-correlation between sidebranching signals extracted on different dendrites shows no correlation for any delay [Fig. 24(b)]. This here too points to an absence of correlation between the sidebranching phases of different bursts.

We thus turn attention to the intrinsic sidebranching coherence of bursts by performing the cross-correlation between an arbitrary burst and the whole signal (Fig. 25). As for symmetric dendrites, we find a series of bursts in which the correlation function reaches significant values. This reveals the internal coherence of sidebranching by bursts together with a common sidebranch frequency and some phase jumps from bursts to bursts.

Asymmetric dendrites thus show a sidebranch dynamics similar to that found on symmetric dendrites despite the absence of sidebranching on the groove that faces the one which emits sidebranches. Conversely, this tends to reject a significant interplay between the sidebranch dynamics of facing grooves in symmetric dendrites, a statement actually supported by the absence of cross-correlations between them [Fig. 9(a)].

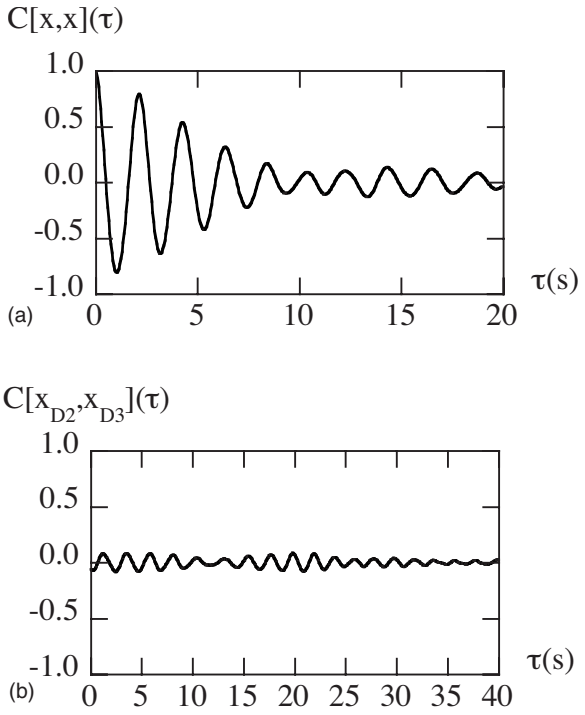

FIG. 24. Correlation functions on asymmetric dendrites. (a) Autocorrelation function of the sidebranching signal. (b) Cross-correlation function between sidebranching signals extracted on different dendrites.

IX. DISCUSSION

We discuss here the main features and implications of our findings. We first stress the steadiness of the dendrite tip motion and we emphasize the absence of relevant extrinsic perturbations for explaining sidebranching coherence. We then conclude about the nature of sidebranching in our system and put it in perspective regarding the literature. We finally draw on possible mechanisms for sidebranching coherence.

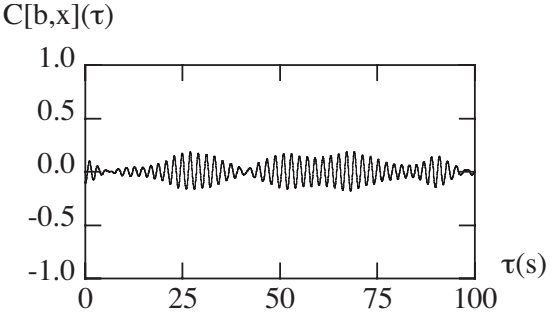

FIG. 25. Cross-correlation function between a burst and the sidebranching signal of an asymmetric dendrite.

A. Steady tip motion

Interestingly, to our optical accuracy, no dendrite tip fluctuation is noticeable on either cells or dendrites at the sidebranching period. The tip position is thus constant within a pixel in the laboratory frame, i.e., to a nominal accuracy of 0.5 μm and, after zooming a factor 4, to an enhanced accuracy of 0.12 μm. The fact that, in the present directional growth experiment, observation of solidification can be made over many sidebranchings in the mean frame of the interface, results in a largely enhanced accuracy on tip velocity. In particular, steadiness of tip position up to 0.5 μm corresponds to a steady velocity to an accuracy on the order of 0.1 μm s^{-1} over a sidebranch emission.

Of course, by definition, one can never exclude tip oscillations below the actual experimental accuracy. For instance, in free growth, a peak at the sidebranching frequency has been found in the frequency spectrum of the tip velocity but its detection has been recognized as an experimental challenge [34]. Here, we nevertheless notice that a tip oscillation, if any, would involve an amplitude smaller than a tenth of micron.

On the opposite, the actual surprise in our observation is that sidebranches do not induce any noticeable effect on tip velocities. Indeed, as sidebranches stand as a definitely large perturbation in the vicinity of the dendrite tip, one might have expected some implications on tip motions, at least at the present accuracy. In this respect, the steadiness of dendrite tip velocity reported here appears quite intriguing and significant.

B. Extrinsic perturbations

In our experimental setup, the extrinsic perturbations of the interface dynamics can come from thermal parts or from the sample translation device. We address below their main features and conclude about their effect on the solidification interface. It will appear that none of them involve the required features to be responsible of the observed dynamical features of sidebranching.

1. Thermal perturbations

Heaters and coolers are electronically regulated to better than a tenth of kelvin over less than a tenth of second. These temperature fluctuations generate damped diffusive thermal waves in the sample which further reach the solidification interface in the middle of the gap g. The damping factor writes $\exp[-(\omega/2\kappa)^{1/2}g/2]$, where ω is the characteristic frequency of fluctuations and κ is the glass diffusivity. Given our gaps, it is smaller than $\exp(-40)$, i.e., 6×10^{-18}. The temperature fluctuations given by the thermal devices at the solidification interface are thus negligible.

Convection between heaters and coolers might yield thermal modulations at the sample surface, whose unsteadiness could induce dynamic perturbations onto the interface. However, their effect has been minimized by inserting thin glass plates above and below the sample so as to delimit a 1-mm-thick layer free of external disturbances. Nevertheless, let us consider the effect of the largest possible temperature fluctuation $\delta T\approx100$ K occurring at the sample surface on a zone typically of the order of the air layer depth δ, i.e., a millimeter. Due to the large thermal conductivity of glass, four times larger than that of air, this perturbation will spread in the glass plate by diffusion over a zone about four times larger. Then, following the low volumetric capacity of air C_a, 2000 times smaller than that of glass C_g, the net mean temperature variation of the perturbed glass zone will be of order $\delta T(C_a/C_g)/16\approx3\times10^{-3}$ K only. For a thermal gradient of 50 K cm^{-1}, this corresponds to a variation in position of about 0.6 μm. This perturbation will eventually be damped by diffusion on a time scale of order $16\delta^2/\kappa\approx30$ s. Its typical extension and time scale thus cannot be linked to sidebranching.

2. Mechanical perturbations

Four kinds of perturbations of the sample translation can be induced in the setup: the screw misalignment, the reductor rotation, the motor steps, and the motor microsteps. The screw misalignment yields a modulation at the period of the screw pitch $l_p=5$ mm. In comparison, the remaining perturbations involve modulation lengths that are reduced according to the cascade: reductor factor 74.1, motor step number 200, and microsteps number 32. This yields the following modulation periods: $l_r=l_p/74.1=67$ μm for the reductor, $l_m=l_p/200=0.33$ μm for the motor steps, and $l_\mu=l_m/32=10^{-2}$ μm for the motor microsteps.

We notice that these perturbation lengths are constant whereas the distance between consecutive sidebranches varies as $l_S=VT_S\propto V^{-0.6}$ [Fig. 6(b)]. Accordingly, these mechanical perturbations can hardly be invoked as responsible for sidebranching. Nevertheless, it appears that the screw and the motor involve a much larger and much smaller modulation length than the sidebranch period l_S, respectively, but that, in between, the reductor displays a perturbation length l_r of the same order: $l_r\approx l_S$ since $50<l_S<150$ μm in our range.

To further analyze the possible effects of mechanical perturbations, we then consider their implication on the thermal field around the interface. This turns out addressing the implications of a modulation $\tilde{V}(t)$ of the velocity V of the sample translation. Owing to the linear form of the advection-diffusion equation which sets the dynamics of the thermal field in the sample, this may be straightforwardly performed by a normal mode analysis. The Appendix then shows that above a velocity of $1.6\kappa l/g^2$, a perturbation of modulation length l leaves the thermal field frozen. This means that it only undergoes a *global* translation at the additional speed $\tilde{V}(t)$ with no other kinds of evolution. The same conclusion can also be made for the concentration field which is advected at the actual sample velocity. Both effects then yield the interface to simply translate at the velocity of the fluctuation $\tilde{V}(t)$ with no other kinds of dynamical evolution.

The above criterion thus states that a dynamical implication of mechanical perturbations on solidification can only be sought below a velocity of 40 μm s^{-1} for the screw, 0.5 μm s^{-1} for the reductor, 3.10^{-3} μm s^{-1} for the motor steps, and 10^{-4} μm s^{-1} for the motor microsteps. Only the screw can then induce a dynamical perturbation on the so-

lidification interface in the velocity range of sidebranching, but on a modulation length extremely large compared to the sidebranching period or the burst length. Conversely, the same criterion shows that perturbations at the sidebranching period l_S, if any, could only have a dynamical effect below 2 μm s^{-1} (Appendix), i.e., far below the occurrence of sidebranching. Accordingly, none of the four possible mechanical perturbations listed above can be part of the sidebranching dynamics.

The same kind of arguments for bursts shows that none of the above mechanical perturbations provide a modulation length of the order of the burst spatial scale $l_B \approx 8 l_S$: $l_r \ll l_B \ll l_p$. On the other hand, a perturbation on this scale would yield no dynamical effects above 7.5 μm s^{-1}, a velocity of the order of the sidebranching onset but far below those considered in the sidebranching regimes. No mechanical perturbation of the sample translation can thus be at the origin of the burst dynamics.

In addition, we stress that mechanical perturbations of the sample velocity, whatever their origin, would nevertheless act the same way and at the same time on the whole interface, i.e., on the whole dendrites. They would then yield the same perturbations of dendrite tip motion, whatever the dendrite, and thus large correlations between the sidebranch dynamics displayed on different dendrites or on different sides of a dendrite. None of these features have been observed here either on sidebranching or on burst dynamics (Secs. IV–VIII). Accordingly, regarding modulation lengths, field dynamics, and spatial coherence, neither thermal nor mechanical perturbations appear to play a role in the observed sidebranching dynamics.

C. Nature of sidebranching coherence

The correlation analyses of sidebranching signals have brought about an ambivalent nature of sidebranching: sidebranch emissions occur by bursts with a large coherence in each burst but no coherence regarding both the burst emission and the burst sidebranching phase. Each burst thus appears as a new dynamical event, internally coherent, but independent of the previous ones, especially regarding the sidebranching phase.

The sidebranching signal thus appears analogous to the succession of wave trains found in natural light: large coherence in each train but complete decorrelation between trains regarding their emission time and their phase. These features yield an absence of statistical coherence unless definite trains are considered. One recovers this way our main results: absence of cross-correlation between extended sidebranching signals, whatever their origin; large cross- or autocorrelation between single bursts, whatever their origin; a coherence time of extended signals close to the mean burst length.

The analogy between sidebranching and natural light emphasizes the nature of the dynamical system responsible for sidebranch emissions. In natural light, the intrinsic coherence of wave trains points to the existence of oscillators involving a large quality factor: the atoms. Here, the intrinsic coherence of sidebranching bursts points to the existence of a limit cycle in the sidebranch dynamics. The fact that coherence is reached as soon as a burst is emitted indicates a large attraction of this limit cycle in phase space. That different bursts show large cross-correlation with no beating reveals a large frequency stability, not only in each burst, but also from burst to burst, whatever their origin.

D. Comparison to literature

Experiments in free [8,9,33,34,36–38,40,41] or directional [35,39] growth have displayed a large range of dynamical behavior for sidebranching including either steady [8,9,36–38] or oscillatory [33–41] tip motions with either sidebranch coherence, at least in some regimes, [36–39] or none [8,9]. We interpret our results below in light of these previous findings.

The steadiness of dendrite tip motion has been noticed on the free growth of a supersaturated NH_4Br aqueous solution [8] and on that of a pure xenon melt [9]. In particular, the relative velocity fluctuations were found less than $\pm 3.5\%$ [8] and $\pm 3\%$ [9], respectively. In the present directional growth experiment, a steady tip velocity was also found to an accuracy of 0.1% over a burst length. Despite these large accuracies, a definite conclusion about tip steadiness relies on the level below which any significant role of tip velocity modulations in sidebranching can be ruled out. Without a definite identification of the sidebranching mechanism, its determination remains an open issue. In particular, in free growth of pure pivalic acid, an accurate study of the frequency spectrum of dendrite tip motion revealed a peak at the sidebranching frequency but with an amplitude weaker than that of the signal noise [34]. Whether this peak is a cause or a consequence of sidebranching and whether its role in sidebranch dynamics is negligible or essential thus remains to elucidate.

Anyway, it nevertheless appears that in these four experiments [8,9,16,34], tip velocity modulation, if any, was extremely tiny in comparison with the sidebranch amplitudes. This provides a definite difference with the tip pulsations found at an amplitude similar to sidebranches in some experiments, at least in some regimes [36–39].

Many of these tip pulsations were related to tip splitting or to a succession of flattening and protruding phases at the tip, actually reminiscent of the early phases of tip splitting. This contrasts with our experiment where no tip oscillation and no tendency to tip splitting were evidenced. It appears, however, that these tip-splitting-like dynamics occurred for specific growth directions of dendrites, namely, the [111] direction [37–39] or the [100] direction with splittings into the [110] direction [36]. They were thus likely linked to anisotropy. Here, our observations are made on dendrites growing in or close to the [100] direction, with sidebranches not ascribed to grow in a direction normal to the dendrite trunk and on a material, the succinonitrile, involving a low interfacial or kinetic anisotropy. Accordingly, one may expect the role of anisotropy to be weaker here, thus possibly preventing the occurrence of these tip-splitting-like modes.

For dendrites involving an oscillatory tip motion, one may expect some sidebranch correlations between their left and right sides. This has been actually noticed in [36] in both a

tip-splitting mode and a tip-oscillating mode (with in this last case both symmetric or antisymmetric dendrite sides), in [37] with observations on three sidebranching periods, in [39] with regular alternate splittings about 80% of times, and in [38] for a moderate velocity regime $20<V<50$ μm s^{-1}. These left/right correlations are at variance with our observation of an absence of cross-correlation between signals extracted on both sides of a dendrite. This difference goes in line with our observation of tip steadiness.

For dendrites involving a steady tip motion, a sidebranch correlation between the left and right sides of a dendrite is more striking. It has been observed on freely growing dendrites from a cross-correlation function between the left and right sides of the same dendrite [8]. There, damped oscillations of the correlation function extended over a coherence time of six sidebranching periods. Judging from the present experiment, this reveals a noticeable coherence between both sides of the dendrite. This statement contrasts with the sidebranching dynamics found here since no cross-correlation was detected between the signals extracted from the two sides of a same dendrite. Similarly, the absence of correlation between the opposite sides of dendrites has been reported on thermal xenon dendrites in support of a fractal analysis of their shape [9].

On a general viewpoint, correlations between the left and right sides of a dendrite indicate common or correlated perturbations of the two dendrite sides presumably generated at the dendrite tip. In the experiments referred in [36–39], they could be naturally traced back to tip oscillations. Without evidence of noticeable tip oscillations in [8], their origin remains more puzzling there.

Intrinsic coherence of sidebranching directly traces back to the autocorrelation of the sidebranching signal on a given side of a dendrite. No such correlation analysis has been achieved on dendrites involving oscillatory tips but dendrite images show a large intrinsic correlation in [36,38]. On the other hand, an autocorrelation extending over six sidebranching periods has been reported on free growth of supersaturated NH_4Br aqueous solution [8]. This appears similar to the coherence time found here on a sidebranching signal but is at variance with the absence of correlation reported on a detailed analysis of sidebranching on thermal xenon dendrites [9].

Altogether, this comparative review shows that no experiment gathers the same observations that those reported here, namely, no tip splitting, no tip oscillation, and no cross-correlation between opposite sides of a dendrite but an autocorrelation of the sidebranching signal pointing to a large coherence by bursts. In particular, all experiments recovered at least one of the above features but none agreed with all and no experiment emphasized the emission of sidebranches by bursts and its implication on sidebranching coherence. However, this specific feature, the existence of sidebranch bursts, deserves to be emphasized for two main reasons. First, because it provides an alternative scenario between a robust nonlinear oscillator and a noisy amplifier: a limit cycle visited erratically at each burst occurrence. Second, because sidebranching dynamics then shows an ambivalence between order (a limit cycle) and disorder (erratic bursts) which may help understanding in a single framework the large range of observations on sidebranching. In particular, we notice that experiments which showed a large cross-correlation between opposite sides of dendrites are also those which involved long sidebranch emissions, i.e., long bursts [36–39]. Conversely, those which concluded to moderate auto- and cross-correlations involved moderately long emissions, i.e., bursts of only several sidebranches [8,16]. As the burst emissions are found here to be erratic and at the origin of a reset of phase coherence, the burst length may thus be a possible explanation of the diversity of the conclusions of experiments on the nature of sidebranching.

E. What mechanisms for a coherence by bursts

Our observations raise two main issues regarding the nature and the mechanisms of sidebranching, one referring to bursts and the other to sidebranches. The first issue refers to the origin of bursts and the reason for their finite lifetime. We first notice that, as bursts occur on asymmetric dendrites on which a single side is branching, their origin cannot be attributed to feedback interactions between the two branching sides of dendrites at their tip. On the other hand, according to the linearized approaches of dendrite dynamics [23–28,32], bursts should correspond to localized wave packets of disturbances initiated in the tip region and evolving down to the tail as the dendrite grows. Their long duration as compared to the coherence time of noise is, however, puzzling and at variance with the statistics of natural noise. In particular, the coherence length of interface fluctuations determined on thermal dendrites [27] would be smaller than a sidebranch spacing here and thus too small to explain the observed burst lengths. Other causes involving nonlinearity seem, therefore, to have to be looked for to explain the burst features.

A possible nonlinear scenario could rely on a subcritical nature of the interface instability yielding amplitude perturbations to relax on a large time. However, burst envelopes show a merely concave shape instead of an overall relaxation profile and no kind of natural perturbation seems to involve the required magnitude to spontaneously generate the observed bursts [26]. Another possibility would be an intermittent character of sidebranching following which the vicinity of a limit cycle emitting sidebranches would be repeatedly visited over finite periods of time. However, the sidebranching signals do not show the usual features of intermittent signals and no values of the control parameters seem to yield a permanent state of oscillations, i.e., an actual limit cycle. In particular, even in the strong sidebranching regime where sidebranches are continuously emitted, the phase jumps that they display indicate that they refer to different wave trains of oscillations. More works are thus required to elucidate the origin of burst dynamics. This would be of primary importance for understanding the reset of sidebranching phase coherence or the phase jumps between bursts and thus the practical limitations for ordered dendritic sidebranching.

The second issue refers to the origin and the mechanism of sidebranching coherence in each burst, till its very beginning to its very end. This, obviously, requires either nonlinear features or coherent perturbations. In particular, as linear mechanisms only add the effects of perturbations, they can

only provide a phase coherence that would already be present in their initial conditions, i.e., in the perturbation bath. Such kind of coherent perturbations have been externally introduced in various studies of forced free [45–47] or directional sidebranching [48]. On natural sidebranching, they could be naturally provided by an alternate dynamical mechanism, as a tip dynamics mediated by the first stage of a tip-splitting instability [36–39]. However, in our experiment, it appears that this tip dynamics, if any, involves amplitudes below our best resolution and thus far below the sidebranch amplitude. A nonlinear mechanism capable of providing coherent sidebranches from erratic noise thus seems mandatory to explain our observations.

A canonical way for providing nonlinearity is a feedback loop. Notice that it must already be at work on the single branching side of asymmetric dendrite. Here, the feedback would link the effect of a sidebranch to the conditions prevailing at the location of its origin, the dendrite tip, or more generally on an upward part of the interface. In both cases, this coupling would thus be nonlocal. Suggestions for such kind of coupling include solute diffusion [40], propagation [31,32], phase diffusion [11], and elasticity [57]. The former mechanism has been proposed for explaining tip oscillations by the perturbations induced by sidebranches on the concentration field [40]. It is actually at work in the oscillatory instability of cells (e.g., $2\lambda - O$ mode), but on diffusive time scales much larger than the sidebranching periods [58–60] and rather of the order of burst lengths. The second suggestion involves two different mechanisms. The first one points to the selection of a propagation velocity of nonlinear fronts sufficiently large to make a sidebranch front propagate back to the vicinity of the dendrite tip [31]. This is reminiscent, in the nonlinear regime, of the possibility of propagation of disturbances back to the tip found in the linear analysis of interfacial waves of thermal dendrites [24–27,32]. In particular, the cubic dispersion relationship inherent to the instability of solidification interfaces (i.e., the Mullins-Sekerka instability [12]) gives rise to three modes among which two propagate toward the dendrite tip and one toward its tail [24–26,32]. Furthermore, the existence of a turning point for the normal linear modes gives rise to a reflection of waves back to the dendrite tip and eventually to their trapping within the tip region [32]. The next mechanism addresses the nonlinear amplitude regime of an unstable curved interface on which the dynamics is then driven by a slow mode: the phase of modulations. It was then observed and derived that nonlinear phase diffusion improves the ordering of phase modulations [11]. Finally, the last mechanism relies on the preferred elastic modes of deformations of a curved substratum [57]. These modes were then invoked as an origin of the well-ordered emission of protrusions on meristems which is known to be a precursor of phyllotaxis [6].

Other mechanisms suitable for yielding a limit cycle for the tip dynamics invoke a combined effect of stretch and nonlinearity [61] or a competition between the surface tension anisotropy and the kinetic anisotropy resulting in an alternance of preferred growth directions [37]. The latter scenario echoes the various structures and growth directions found in free growth when varying the relative magnitude of the two kinds of anisotropy [62]. It is also reminiscent of the limit cycle found in a geometrical model of growth interface in which a higher derivative mimics the effect of anisotropy [30].

Many physical phenomena can thus possibly yield a limit cycle for sidebranching provided a nonlocal feedback is worked out in the growth system. However, the right mechanism will have to provide sidebranch coherence as soon as sidebranches are emitted and avoid tip oscillations at least to the accuracy of the present study, i.e., to less than about 2% of the typical sidebranch amplitude.

Interestingly, we notice that, according to several scenarios, the mechanism for sidebranch coherence could rely on extremalization: the elastic scenario where the less energetical deformation selects a triad of modes [57], the phase diffusion scenario where regularity corresponds to the minimum of a Liapunov functional [11], and the anisotropy scenario [37] where the preferred growth direction satisfies a minimum undercooling [62]. In such cases, sidebranching coherence would then simply appear as an optimal state of growth.

X. CONCLUSION

Correlation analyses of dendritic sidebranching in directional solidification have revealed different levels of organization depending on time scales. At large times, sidebranching appears erratically emitted by bursts involving no coherence in occurrence or length. At small times, sidebranching shows a surprisingly large level of coherence in all bursts over their whole duration. This coherence is, nevertheless, restricted to each burst since phase correlation is lost at the transition between bursts.

No spatial correlation appeared on the solidification interface regarding burst occurrence, burst length, or sidebranching phase. However, the large intrinsic coherence of sidebranching in all bursts provided large cross-correlations between single bursts, whatever the dendrite or the dendrite side to which they belong.

These features remained valid in both the moderate sidebranching regime and the strong sidebranching regime, even if in the latter the bursts overlapped. Then, the sidebranching phase enabled the identification of burst transitions as phase steps.

Altogether, these results bring about a balanced view on sidebranching organization: well organized sidebranches within uncorrelated bursts emitted erratically. This actually appears reminiscent of the organization of natural light: a large coherence due to atom organization within uncorrelated wave trains due to different sources of emissions. Similarly, the large coherence of sidebranching in bursts points to a deterministic origin for explaining the existence of such a limit cycle and to a stochastic origin for explaining burst uncorrelation.

The origin of a limit cycle for sidebranch emission has to be traced back to physical couplings on dendrites. However, their mechanisms could hardly involve the dynamics of dendrite tips since they proved to be fairly steady here in the thermal gradient frame. Other kinds of scenarios are at present speculative and require further inquiry. Identifying

them might provide tools for improving the order of crystalline solidified materials or, on a more general viewpoint, evidence generic mechanisms of coherence relevant to other kinds of branching phenomena.

APPENDIX: EFFECT OF VELOCITY FLUCTUATIONS ON THE THERMAL FIELD

We address the effect on the thermal field of a perturbation $\tilde{V}(t)$ of the pulling velocity V involving no long-time average. This, therefore, corresponds to a sample translation whose regularity is perturbed but which keeps the same average V over a long time.

We especially seek to determine the conditions for which the thermal field will be adiabatically advected with the perturbation with no other dynamical evolutions. In this case, as the concentration field will also be simply globally advected, the growth conditions will be unchanged in the frame comoving with the perturbation. The solidification interface will then simply be translated back and forth by the perturbation without changing dynamics.

In the laboratory frame, the thermal field $T(z,t)$ satisfies an advection-diffusion equation,

$$\frac{\partial T}{\partial t} + \mathbf{V}\cdot\boldsymbol{\nabla} T = \kappa \Delta T, \tag{A1}$$

where $\kappa = 5\times 10^5$ μm^2 s^{-1} denotes the diffusivity of glass. Here, the diffusivity of the melt can be neglected owing to its small depth (50 μm) compared to the glass plates thickness (1 mm). The boundary conditions are $T(0,t)=T_0$, $T(g,t)=T_0+Gg$, where g denotes the gap between heaters and coolers and G the mean thermal gradient. In particular, we note that $\mathbf{G}=G\mathbf{e}_z$ and $\mathbf{V}=-V\mathbf{e}_z$ with positive V and G.

The steady-state solution T_s for the temperature field reads

$$T_s(z) = Gg\frac{1-\exp(-\mathrm{Pe}\, z/g)}{1-\exp(-\mathrm{Pe})} + T_0, \tag{A2}$$

where $\mathrm{Pe}=Vg/\kappa$ denotes the thermal Péclet number of the system. We note that it will be convenient later on to write it in terms of a diffusion velocity $V_d=\kappa/g$: $\mathrm{Pe}=V/V_d$. We finally stress that Pe is low in our experiment: $\mathrm{Pe}\lesssim 1/2$. For instance, for $g=10$ mm, $V_d=50$ μm s^{-1}, so that, for $V<30$ μm s^{-1}, $\mathrm{Pe}<0.6$.

We now consider a perturbation $\tilde{V}(t)$ of the pulling velocity and denote $\tilde{z}(t)$ the corresponding perturbation of the sample position. We analyze its effect in the frame $\tilde{R}$ comoving with the perturbation, i.e., in the frame translated by $\tilde{z}(t)$ with respect to the laboratory frame. We note $\hat{T}$ and $\hat{z}$ the temperature field and the positions seen in this new frame.

In the frame $\tilde{R}$, the sample keeps translating at the velocity $\mathbf{V}$ so that its thermal field $\hat{T}(\hat{z},t)$ keeps satisfying the advection-diffusion Eq. (A1). However, the thermal boundary conditions are changed at the dominant order into $\hat{T}(0,t)=\max[T_s(\tilde{z}),T_0]$ and $\hat{T}(g,t)=\min[T_s(g+\tilde{z}),T_0+Gg]$. Disregarding harmonics, we shall assimilate them to $\hat{T}(0,t)=T_s(\tilde{z})$ and $\hat{T}(g,t)=T_s(g+\tilde{z})$.

To analyze the effect of these perturbed boundary conditions, we decompose $\hat{T}$ into the steady field T_s and a deviation $\tilde{T}$ of the order of the imposed perturbation: $\hat{T}=T_s+\tilde{T}$. The field $\tilde{T}$ satisfies also Eq. (A1) but with the modified boundary conditions: $\tilde{T}(0,t)=T_s(\tilde{z})-T_s(0)=G(0)\tilde{z}$ and $\tilde{T}(g,t)=T_s(g+\tilde{z})-T_s(g)=G(g)\tilde{z}$ where $G(0)$ and $G(g)$ denote the actual thermal gradient dT_s/dz at $z=0$ and $z=g$:

$$G(0) = \frac{\mathrm{Pe}\, G}{1-\exp(-\mathrm{Pe})}, \quad G(g) = \exp(-\mathrm{Pe})G(0). \tag{A3}$$

To solve the advection-diffusion equation in $\tilde{T}$ with the above boundary conditions, we apply a normal mode analysis and write $\tilde{z}=z_0\exp(i\omega t)$, $\tilde{V}=V_0\exp(i\omega t)$, and $\tilde{T}=\exp(i\omega t)[T_+\exp(ik_+\hat{z})+T_-\exp(ik_-\hat{z})]$. The boundary conditions yield a linear system in (T_+,T_-) whose solution is

$$(T_+,T_-) = z_0G(0)[\exp(ik_+g)-\exp(ik_-g)]^{-1} \times[\exp(-\mathrm{Pe})-\exp(ik_-g),\exp(ik_+g)-\exp(-\mathrm{Pe})]. \tag{A4}$$

We then notice that we are actually interested in the temperature field in the vicinity of the solidification interface, i.e., at about the melting temperature T_M. As the temperatures of the thermal devices have been taken symmetric with respect to T_M, the melting temperature keeps being reached at $\hat{z}\approx g/2$ in our low Péclet number regime (the approximation is better than 15% for $\mathrm{Pe}<1/2$). The perturbed temperature then writes there:

$$\hat{T}(g/2,t) = z_0\exp(i\omega t)G(g/2)\exp(\mathrm{Pe}/2) \times\frac{\exp(-\mathrm{Pe})+\exp[i(k_++k_-)g/2]}{\exp(ik_+g/2)+\exp(ik_-g/2)}. \tag{A5}$$

The modes (k_+,k_+) are solutions of the dispersion relation of Eq. (A1). They write

$$k_+ = \frac{\omega}{\mu V} + i\frac{V}{2\kappa}(1-\mu), \tag{A6}$$

$$k_- = -\frac{\omega}{\mu V} + i\frac{V}{2\kappa}(1+\mu), \tag{A7}$$

with $2\mu^2=1+(1+16\Omega^2)^{1/2}$ and $\Omega=\omega\kappa/V^2$.

In relation (A5), the term $z_0\exp(i\omega t)G(g/2)$ corresponds to the temperature modulation $\tilde{T}_a$ that would be undergone in the comoving frame $\tilde{R}$ if the temperature field would remain steady in the laboratory frame. We shall use it to interpret the magnitude of $\hat{T}(g/2,t)$ and decide if an adiabatic translation by the velocity perturbation is satisfied. We thus introduce the following criterion for this adiabatic translation to be satisfied: $|\hat{T}(g/2,t)|\ll|\tilde{T}_a|$.

We now notice that

$$\frac{\hat{T}(g/2,t)}{\tilde{T}_a} = \frac{\cosh(\mathrm{Pe}/4)}{\cosh[\mathrm{Pe}\ \mu/4 + i\omega g/(2\mu V)]} \tag{A8}$$

so that $|\hat{T}(g/2,t)| \approx |\tilde{T}_a| \exp[\mathrm{Pe}(1-\mu)/4]$. The criterion for adiabatic translation then reduces to $\mathrm{Pe}(\mu-1) > 4$ and, as $\mathrm{Pe} \lesssim 1/2$, to $\mathrm{Pe}\ \mu > 4.5$.

Let us apply this criterion to the three mechanical perturbations inherent to our translation device: the screw misalignment, the motor step, and the motor microstep. We label l the distance made by the sample on a period of perturbation, i.e., respectively, $l_p = 5$ mm (the screw pitch) at each screw turn, $l_r = l_p/74.1$ at each reductor turn, $l_m = l_r/200$ at each motor step, and $l_\mu = l_m/32$ at each motor microsteps. Then $\omega = 2\pi V/l$ and $\Omega = 2\pi V_l/V$ with $V_l = \kappa/l$. As V_l is larger than 100 μm s^{-1} here, it appears that Ω is large enough for the criterion $\mathrm{Pe}\ \mu > 4.5$ to reduce to $V > 1.6 V_d l/g$, i.e., $V > 1.6\kappa l/g^2$. Above the velocity $1.6\kappa l/g^2$, perturbations on the characteristic distance l will thus translate the sample adiabatically back and forth with no implication on the thermal field seen by the growth interface and, thus, on solidification.

[1] J. Dumais and D. Kwiatkowska, Plant J. **31**, 229 (2002).
[2] M. B. Short, J. C. Baygents, and R. E. Goldstein, Phys. Fluids **18**, 083101 (2006).
[3] P. G. Saffman and G. I. Taylor, Proc. R. Soc. London, Ser. A **245**, 312 (1958).
[4] S. C. Huang and M. E. Glicksman, Acta Metall. **29**, 701 (1981).
[5] C. Pelcé-Savornin, J. Quinard, and G. Searby, Combust. Sci. Technol. **58**, 337 (1988).
[6] A. Douady and Y. Couder, J. Theor. Biol. **178**, 255 (1996).
[7] M. E. Glicksman, R. J. Schaefer, and J. D. Ayers, Metall. Trans. A **7**, 1747 (1976).
[8] A. Dougherty, P. D. Kaplan, and J. P. Gollub, Phys. Rev. Lett. **58**, 1652 (1987).
[9] U. Bisang and J. H. Bilgram, Phys. Rev. E **54**, 5309 (1996).
[10] E. O. Budrene and H. C. Berg, Nature (London) **376**, 49 (1995).
[11] S. Bottin-Rousseau and A. Pocheau, Phys. Rev. Lett. **87**, 076101 (2001); A. Pocheau and S. Bottin-Rousseau, Chaos **14**, 882 (2004).
[12] W. W. Mullins and R. F. Sekerka, J. Appl. Phys. **35**, 444 (1964).
[13] S. H. Davis, *Theory of Solidification* (Cambridge University Press, Cambridge, England, 2001).
[14] W. Kurz and D. J. Fischer, *Fundamentals of Solidification* (Transtech Publications Ltd., Uetikon-Zurich, Switzerland, 1998).
[15] S. Deville, E. Saiz, R. K. Nalla, and A. Tomsia, Science **311**, 515 (2006).
[16] M. Georgelin, S. Bodea, and A. Pocheau, Europhys. Lett. **77**, 46001 (2007).
[17] C. Ribak and L. Shapiro, Brain Res. **55**, 390 (2007).
[18] M. Rosso, E. Chassaing, V. Fleury, and J.-N. Chazalviel, J. Electroanal. Chem. **559**, 165 (2003).
[19] *Branching in Nature*, edited by V. Fleury, J.-F. Gouyet, and M. Léonetti (EDP Sciences, Les Ulis; Springer, Berlin, Heidelberg, 2000).
[20] J. S. Langer, Rev. Mod. Phys. **52**, 1 (1980).
[21] M. Georgelin and A. Pocheau, Phys. Rev. E **57**, 3189 (1998).
[22] Ya. B. Zel'dovich, A. G. Istratov, N. I. Kidin, and V. B. Librovich, Combust. Sci. Technol. **24**, 1 (1980).
[23] P. Pelcé and P. Clavin, Europhys. Lett. **3**, 907 (1987).
[24] R. Pieters and J. S. Langer, Phys. Rev. Lett. **56**, 1948 (1986).
[25] M. N. Barber, A. Barbieri, and J. S. Langer, Phys. Rev. A **36**, 3340 (1987).
[26] J. S. Langer, Phys. Rev. A **36**, 3350 (1987).
[27] E. Brener and D. Temkin, Phys. Rev. E **51**, 351 (1995).
[28] S. K. Sarkar, Phys. Lett. A **117**, 137 (1986).
[29] O. Martin and N. Goldenfeld, Phys. Rev. A **35**, 1382 (1987).
[30] D. A. Kessler, J. Koplik, and H. Levine, Phys. Rev. A **30**, 3161 (1984).
[31] W. Van Saarloos, B. Caroli, and C. Caroli, J. Phys. I **3**, 741 (1993).
[32] J.-J. Xu, Phys. Rev. A **43**, 930 (1991).
[33] E. Rolley, S. Balibar, and F. Gallet, Europhys. Lett. **2**, 247 (1986).
[34] J. C. LaCombe, M. B. Koss, J. E. Frei, C. Giummarra, A. O. Lupulescu, and M. E. Glicksman, Phys. Rev. E **65**, 031604 (2002).
[35] L. R. Morris and W. C. Winegard, J. Cryst. Growth **1**, 245 (1967).
[36] H. Honjo, S. Ohta, and Y. Sawada, Phys. Rev. Lett. **55**, 841 (1985).
[37] Y. Sawada, B. Perrin, P. Tabeling, and P. Bouissou, Phys. Rev. A **43**, 5537 (1991).
[38] Y. Couder, J. Maurer, R. González-Cinca, and A. Hernández-Machado, Phys. Rev. E **71**, 031602 (2005).
[39] B. Utter, R. Ragnarsson, and E. Bodenschatz, Phys. Rev. Lett. **86**, 4604 (2001); B. Utter and E. Bodenschatz, Phys. Rev. E **66**, 051604 (2002).
[40] E. Raz, S. G. Lipson, and E. Polturak, Phys. Rev. A **40**, 1088 (1989).
[41] V. Ferreiro, J. F. Douglas, J. Warren, and A. Karim, Phys. Rev. E **65**, 051606 (2002).
[42] M. Rabaud, Y. Couder, and N. Gerard, Phys. Rev. A **37**, 935 (1988).
[43] P. Huerre, *Perspectives in Fluid Dynamics* (Cambridge University Press, Cambridge, England, 2000), pp. 159–229.
[44] J.-M. Chomaz, Phys. Rev. Lett. **69**, 1931 (1992).
[45] P. Bouissou, A. Chiffaudel, B. Perrin, and P. Tabeling, Europhys. Lett. **13**, 89 (1990).
[46] T. Börzsönyi, T. Tóth-Katona, Á. Buka, and L. Gránásy, Phys. Rev. E **62**, 7817 (2000).
[47] M. Fell and J. Bilgram, Phys. Rev. E **75**, 061603 (2007).
[48] X. W. Qian and H. Z. Cummins, Phys. Rev. Lett. **64**, 3038 (1990); L. M. Williams, M. Muschol, X. Qian, W. Losert, and H. Z. Cummins, Phys. Rev. E **48**, 489 (1993).
[49] J. D. Weeks, W. Van Saarloos, and M. Grant, J. Cryst. Growth

112, 244 (1991).
[50] B. Billia and R. Trivedi, *Handbook of Crystal Growth* (Elsevier Science Publishers, New York, 1993), Vol. 1, Chap. 14.
[51] A. Pocheau and M. Georgelin, J. Phys. IV **11**, 169 (2001).
[52] A. Pocheau and M. Georgelin, J. Cryst. Growth **250**, 100 (2003).
[53] A. Pocheau and M. Georgelin, Phys. Rev. E **73**, 011604 (2006).
[54] M. Georgelin and A. Pocheau, J. Cryst. Growth **268**, 272 (2004).
[55] M. Georgelin and A. Pocheau, *Branching in Nature*, edited by V. Fleury, J.-F. Gouyet, and M. Léonetti (EDP Sciences, Les Ulits; Springer, Berlin, Heidelberg, 2001), pp. 409–415.
[56] J. Deschamps, M. Georgelin, and A. Pocheau, Europhys. Lett. **76**, 291 (2006); A. Pocheau, J. Deschamps, and M. Georgelin, JOM **59**, 71 (2007); J. Deschamps, M. Georgelin, and A. Pocheau, Phys. Rev. E **78**, 011605 (2008).
[57] P. D. Shipman and A. C. Newell, Phys. Rev. Lett. **92**, 168102 (2004).
[58] M. Georgelin and A. Pocheau, Phys. Rev. Lett. **79**, 2698 (1997).
[59] A. Karma and P. Pelcé, Phys. Rev. A **39**, 4162 (1989).
[60] P. Kopczynski, W.-J. Rappel, and A. Karma, Phys. Rev. Lett. **77**, 3387 (1996).
[61] P. Pelcé (unpublished).
[62] T. Haxhimali, A. Karma, F. Gonzales, and M. Rappaz, Nature Mater. **5**, 660 (2006).